The Bioscan
AN INTERNATIONAL QUARTERLY JOURNAL OF LIFE SCIENCES
21(1): 732-759, 2026 www.thebioscan.com

Design, Antioxidant Evaluation and in Silico Anticancer Profiling of Novel Quinoline Derivatives Targeting Apoptosis, Angiogenesis and Metastasis

Pradeepa Kumar C[1], B. T. Prabhakar[2], N. D. Satyanarayan[3], Rajeshwara Achur[1,4*]

[1]Department of Biochemistry, Jnana Sahyadri, Kuvempu University, Shankaraghatta, 577451 Shimoga, Karnataka, India
[2]Molecular Biomedicine Laboratory, Post Graduate Department of Studies and Research in Biotechnology, Sahyadri Science College, Kuvempu University, Shivamogga 577 203, Karnataka, India
[3]Department of Pharmaceutical Chemistry, Post-Graduate Centre, Kuvempu University, Kadur, 577548 Chikmagalur Dist, Karnataka, India
[4]INTI International University, Putra Nilai, Malaysia

Corresponding Author: Rajeshwara Achur, Email: rajachur@gmail.com

DOI: 10.63001/tbs.2026.v21.i01.pp732-759

KEYWORDS
Quinoline derivatives; Anticancer activity; Antioxidant activity; Molecular dynamics simulation; In silico studies

Received on:
16-11-2025

Accepted on:
11-12-2025

Published on:
29-1-2026

Abstract

Quinoline-based scaffolds continue to attract significant interest in anticancer drug discovery due to their structural versatility and broad spectrum of biological activities. In this study, five novel quinoline compounds (QCs) were synthesized and evaluated for their antioxidant and anticancer potential using in vitro assays and in silico approaches. Antioxidant activity was assessed using DPPH and ABTS radical scavenging assays, where all compounds exhibited concentration-dependent activity. At 500 µg/mL, QC-1 demonstrated the highest DPPH radical scavenging activity (69.88 ± 2.90%), while QC-2 showed the greatest ABTS scavenging activity (75.11 ± 2.40%). Molecular docking studies revealed strong binding affinities of all quinoline derivatives toward key cancer-related targets, including BAX, Bcl-2, p53, VEGF, MMP-2 and MMP-9, in comparison to the reference drug 5-fluorouracil. Furthermore, molecular dynamics simulation identified QC-4 as the most stable ligand–protein complex, highlighting its potential as a lead anticancer candidate. Notably, QC-3 exhibited the most favourable multi-target binding profile, suggesting its ability to modulate apoptosis, angiogenesis and metastasis pathways. Overall, the combined antioxidant and in silico findings indicate that quinoline derivatives, particularly QC-3 and QC-4, represent promising multifunctional scaffolds for further anticancer drug development.

1. INTRODUCTION

In drug discovery, quinoline derivatives represent a versatile and valuable scaffold due to their aromatic π-bicyclic, electron-rich structure, which facilitates strong interactions with diverse biological targets in medicinal chemistry [1,2]. In recent years, quinoline-based compounds have attracted considerable attention for their broad pharmacological potential, particularly in oncology [3]. Several quinoline derivatives have demonstrated significant anticancer activity across multiple cancer models through mechanisms including kinase inhibition, disruption of tubulin polymerization, interference with topoisomerase function, induction of apoptosis, cell-cycle arrest and suppression of angiogenesis [4].

In addition to their anticancer effects, numerous quinoline analogues have exhibited potent antioxidant and free radical-scavenging activities in both *in vitro* and *in silico* studies. This dual functionality is especially promising, as oxidative stress plays a critical role in cancer initiation, progression and therapeutic resistance [3]. Cancer cells typically generate excessive levels of reactive oxygen species (ROS), which contribute to genomic instability and tumor growth. Consequently, compounds capable of modulating oxidative stress while exerting anticancer effects may offer enhanced therapeutic benefits. Our previously published *in vitro* and in vivo studies demonstrated the significant anticancer potential of the synthesized quinoline compounds (QCs) [5]. Building on these findings, the present study aims to further elucidate their molecular mechanisms by evaluating their antioxidant properties and in silico anticancer profiles.

Combining antioxidant and anticancer assessments represents a rational strategy for identifying multifunctional therapeutic candidates. *In vitro* radical-scavenging assays, such as DPPH and ABTS, along with *in silico* redox-based analyses, provide insights into electron or hydrogen transfer capacity and overall redox stability [6]. When integrated with molecular docking and molecular dynamics simulations, these approaches enable a comprehensive understanding of structure–activity and structure–redox relationships, revealing the influence of substituent effects on molecular stability, electronic distribution, and biological interactions.

Advances in computer-aided drug design (CADD) have significantly improved early-stage drug discovery by enabling rapid, cost-effective evaluation of biological activity and pharmacokinetic behavior. Structure and ligand-based computational methods, supported by cheminformatics tools, help reduce experimental attrition rates. Early prediction of absorption, distribution, metabolism and excretion (ADME) properties is particularly crucial. In this context, the ADME profiles of the synthesized quinoline derivatives were previously assessed using established computational tools, including Lipinski's Rule of Five and SwissADME and were found to exhibit favorable drug-likeness and physicochemical properties [7]. To further clarify the molecular basis of biological activity, the present study integrates detailed molecular docking and molecular dynamics simulations targeting key cancer-related proteins with *in vitro* and *in silico* antioxidant evaluations. This comprehensive approach aims to identify quinoline derivatives with dual anticancer and redox-modulating activity, balanced pharmacokinetic profiles, and strong target affinity, thereby highlighting promising lead candidates for further medicinal chemistry optimization.

2. MATERIALS

Materials for *In Vitro* Studies

The chemicals used for the *in vitro* antioxidant assays included 2,2′-azinobis(3-ethylbenzothiazoline-6-sulfonic acid) (ABTS), 2,2-diphenyl-1-picrylhydrazyl (DPPH), ethanol, potassium persulfate, and ascorbic acid. The synthesized quinoline compounds (QC-1 to QC-5) were also used in these experiments. All the chemicals were procured from Sigma-Aldrich (Merck, USA) and were of analytical grade.

3. METHODS

DPPH Radical Scavenging Assay

Materials for *In Silico* Studies

The synthesized quinoline compounds (QC-1 to QC-5) were used for computational analyses. Molecular structures were drawn and optimized using ChemDraw Ultra 12.0 and ChemSketch. Molecular docking and visualization were performed using Discovery Studio 2024 Client, Swiss-PDB Viewer, Open Babel and PyRx. The three-dimensional crystal structures of cancer-related target proteins were retrieved from the Protein Data Bank (PDB). These included catalytic domain (PDB ID: 7XGJ) and human matrix metalloproteinase-9 (MMP-9; PDB ID: 1L6J). Molecular dynamics simulations were performed using GROMACS version 2022.4. Ligand topology files were generated using the CHARMM General Force Field (CGenFF) server and long-range electrostatic interactions were calculated using the Particle Mesh Ewald (PME) method.

The DPPH radical scavenging activity was evaluated according to the method described previously [8]. Briefly, 50 µL of the sample solution at concentrations ranging from 10 to 500 µg/mL was mixed with 300 µL of a 0.5 mM DPPH solution prepared in ethanol. The reaction mixture was incubated in the dark at 37 °C for 5 min. Following incubation, the absorbance was measured at 517 nm against a blank using a spectrophotometer. Ascorbic acid was used as the reference standard. The radical scavenging activity of the quinoline compounds (QC-1 to QC-5) was expressed as percentage inhibition and calculated using the following equation:

%Inhibition = (absorbance control-absorbance test)/(Absorbance control) × 100

ABTS Radical Cation Decolorization Assay

The ABTS radical cation decolorization assay was performed as described previously [9]. The $ABTS^{+}$• radical solution was generated by mixing 7mM ABTS with 2.45mM potassium persulfate in a 1:1 (v/v) ratio and allowing the reaction to proceed for 16–20 h at room temperature in the dark. The resulting $ABTS^{+}$• solution was diluted with methanol to obtain an absorbance of 0.70 ± 0.02 at 734 nm. To evaluate antioxidant activity, different concentrations of the synthesized quinoline derivatives (10–500 µg/mL) were added to 3.995 mL of the $ABTS^{+}$• solution and incubated for 30 min at room temperature. The decrease in absorbance was then recorded at 734 nm. Ascorbic acid was used as the positive control. The percentage inhibition of ABTS radicals was calculated using the following equation:

%Inhibition = (absorbance control-absorbance test)/(Absorbance control) × 100

4. MOLECULAR DOCKING STUDIES

Preparation of Proteins and Ligands

Target protein structures were retrieved in PDB format from the RCSB Protein Data Bank. Protein preparation was carried out using Discovery Studio 2024, wherein crystallographic water molecules, heteroatoms and co-crystallized ligands were removed. The prepared protein structures were subsequently saved in PDB format. The chemical structures of the synthesized quinoline compounds (QC-1 to QC-5) were drawn using ChemDraw Ultra 12.0 and ChemSketch software. The structures were energy-minimized and converted into three-dimensional PDB format using Discovery Studio 2024 for subsequent docking studies [10].

Protein-Ligand Interaction Analysis

Molecular docking was performed using PyRx to investigate the binding interactions of the synthesized quinoline compounds and the reference drug 5-fluorouracil (5-FU) with selected cancer-related protein targets. Docking was carried out under standard parameters, and binding affinity scores were generated for each protein-ligand complex. The docked conformations were visualized and analyzed using Discovery Studio 2024 client to elucidate key molecular interactions, including hydrogen bonding, hydrophobic interactions, π-π stacking, and the involvement of critical active-site residues. Particular emphasis was placed on identifying interaction patterns relevant to apoptosis, angiogenesis, and metastasis-related pathways. These in silico analyses provide mechanistic insights into the binding potential of the synthesized quinoline derivatives and support their prospective antioxidant and anticancer activity, offering a rational basis for further experimental validation and lead optimization [10].

Molecular Dynamics (MD) Simulation

The three-dimensional structure of the target protein was obtained from the Protein Data Bank (PDB). Molecular dynamics (MD) simulations were performed for 100 ns to evaluate the structural stability and binding behavior of the selected protein-ligand complexes. All simulations were conducted using the GROMACS 2022.4 software package [12] with the CHARMM36 force field [11]. Ligand topology and parameter files were generated using the CHARMM General Force Field (CGenFF) server [13]. Long-range electrostatic interactions were calculated using the Particle Mesh Ewald (PME) method [14]. Each protein-ligand complex was solvated in a dodecahedral simulation box using the TIP3P water model, maintaining a minimum buffer distance of 1.0 nm between the solute and box edges [15]. System neutrality was achieved by adding appropriate numbers of Na^+ and Cl^- ions. Energy minimization was carried out using the steepest descent algorithm for 5,000 steps to remove steric clashes and unfavorable contacts. The LINCS algorithm [16] was applied to constrain all covalent bonds involving hydrogen atoms. The system was gradually heated to 310 K, followed by two equilibration phases: a 1 ns NVT (constant number of particles, volume, and temperature) equilibration and a subsequent 1 ns NPT (constant number of particles, pressure, and temperature) equilibration. Temperature coupling was maintained using the velocity-rescaling thermostat [17], while pressure coupling was achieved using the Parrinello-Rahman barostat [18]. Following equilibration, a 100 ns production MD simulation was performed under periodic boundary conditions. Trajectory analysis was conducted using built-in GROMACS tools, focusing on structural and conformational stability parameters, including root mean square deviation (RMSD), root mean square fluctuation (RMSF), solvent-accessible surface area (SASA), radius of gyration (Rg) and hydrogen bond analysis.

Free Energy Landscape (FEL) Analysis

The free energy landscape (FEL) approach was employed to investigate protein conformational dynamics and energy minima associated with ligand binding [19]. FEL analysis enables visualization of both stable (low-energy minima) and transient (energy barriers) conformational states, providing insights into biomolecular recognition, folding, and stability.

The Gibbs free energy (G) was calculated using the following equation:

$$\Delta G(X) = -kBT \ln P(X)$$

where *G* represents Gibbs free energy, *kB* is the Boltzmann constant, *T* is the absolute temperature, *X* denotes the reaction coordinate, and *P(X)* is the probability distribution along the reaction coordinate.

MM/GBSA Binding Free Energy Calculations

The binding free energy of the protein-ligand complexes was estimated using the Molecular Mechanics/Generalized Born Surface Area (MM/GBSA) approach implemented via the *gmx_MMPBSA* plugin integrated with GROMACS [20,21]. Binding free energy calculations were performed using trajectory frames extracted from the 0–77 ns interval of the molecular dynamics simulation.

The binding free energy (ΔG_binding) was calculated according to the following equations:

$$\Delta G = G\_(complex\ ) - [\ G\_receptor + G_{ligand}\ ] \quad (1)$$

$$\Delta G_{binding} = \Delta H - T\Delta S \quad (2)$$

$$\Delta H = \Delta G_{GAS} + \Delta G_{SOLV} \quad (3)$$

$$\Delta G_{GAS} = \Delta E_{EL} + \Delta E_{VDWAALS} \quad (4)$$

$$\Delta G_{SOLV} = \Delta E_{GB} + \Delta E_{SURF} \quad (5)$$

$$\Delta E_{SURF} = \gamma . SASA \quad (6)$$

Statistical Analysis

All experimental results are expressed as mean ± standard error (SE), and *in vitro* assays were performed in triplicate. Statistical analysis was conducted using GraphPad Prism version 9. One-way analysis of variance (ANOVA), followed by Tukey's post hoc multiple comparison test, was applied to determine statistical significance among groups. A p value of < 0.05 was considered statistically significant, while p < 0.01 was considered highly significant.

4. RESULTS AND DISCUSSION

Antioxidant Activity of QC-1 to QC-5 (DPPH and ABTS Assays)

The antioxidant potential of the synthesized quinoline compounds (QC-1 to QC-5) was evaluated using DPPH and ABTS radical scavenging assays at concentrations ranging from 100 to 500 µg/mL, with ascorbic acid serving as the reference standard. Both assays revealed a clear concentration-dependent increase in radical scavenging activity, confirming the inherent antioxidant capacity of the quinoline scaffold.

In the DPPH assay, scavenging activity at 100 µg/mL ranged from 14.99% (QC-5) to 26.30% (QC-4). Activity increased with concentration, reaching 45.21% (QC-4), 44.40% (QC-1), and 42.40% (QC-2) at 300 µg/mL. At 500 µg/mL, QC-1 exhibited the highest DPPH scavenging activity (69.88 ± 2.90%), followed by QC-4 (61.33 ± 1.11%) and QC-2 (57.73 ± 1.22%). In comparison, ascorbic acid displayed 94.84 ± 2.81% inhibition, highlighting the role of multiple hydroxyl groups in enhancing radical neutralization.

On the other hand, the ABTS assay showed higher scavenging efficiencies, particularly at elevated concentrations. At 100 µg/mL, inhibition ranged from 8.20% (QC-3) to 37.36% (QC-4). At 300 µg/mL, QC-2 (56.28%) and QC-4 (54.81%) demonstrated superior activity relative to other derivatives. At 500 µg/mL, QC-2 was the most potent ABTS scavenger (75.11 ± 2.40%), followed by QC-4 (68.01 ± 3.84%) and QC-5 (64.43 ± 2.94%), whereas ascorbic acid reached 97.42 ± 1.91% inhibition.

QC-1 and QC-4 performed best in the DPPH assay, while QC-2 and QC-4 were superior in the ABTS assay. This variation can be attributed to the distinct reaction mechanisms: DPPH primarily measures hydrogen atom transfer, whereas ABTS involves both hydrogen atom and single-electron transfer processes [22]. The enhanced ABTS activity of QC-2 and QC-4 likely reflects more effective electron delocalization, facilitated by extended π-conjugation and electron-donating substituents in their structures.

Overall, the results are consistent with previous reports on quinoline-based antioxidants [23,24], demonstrating that radical-scavenging ability is governed by hydrogen atom donation and electron transfer, both of which are influenced by substituent type and electronic distribution within the quinoline framework

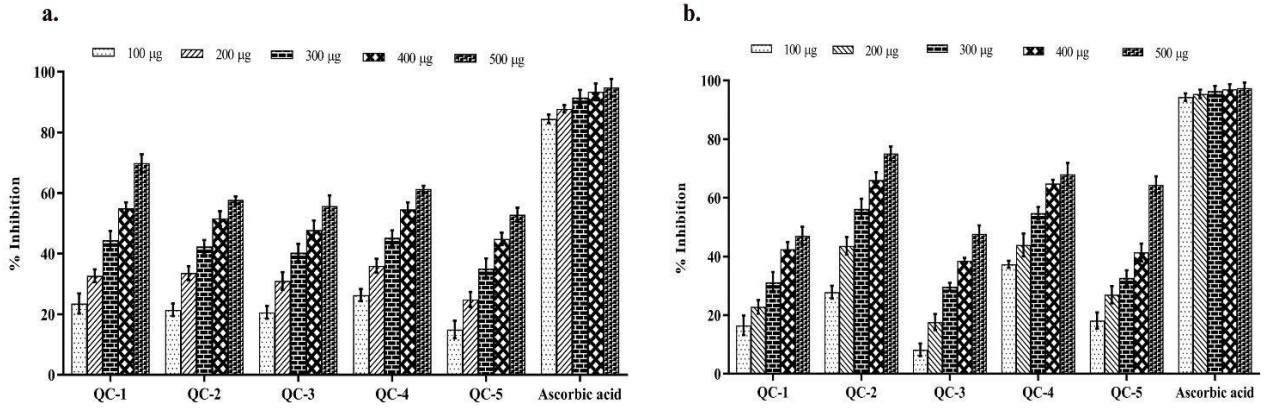

Figure 1. Antioxidant activity of synthesized quinoline derivatives. Bar graphs depicting the percentage radical scavenging activity of QC compounds measured by (a) DPPH and (b) ABTS assays at varying concentrations, compared with the standard antioxidant ascorbic acid. All compounds exhibited a concentration-dependent increase in scavenging activity. Data are presented as mean ± standard deviation (SD) from three independent experiments (n = 3). Statistical significance was evaluated using one-way ANOVA followed by Tukey's post hoc test. Asterisks denote significant differences relative to the control or standard: p < 0.05 (*) and p < 0.01 (**).

Molecular Docking Analysis of Quinoline Compounds Against Cancer-Related Targets

Extensive molecular docking studies were performed for the synthesized quinoline derivatives (QC-1–QC-5) against key apoptosis- and metastasis-associated protein targets, including Bcl-2 (PDB ID: 1G5M), BAX (1F16), BAD (2BZW), p53 (2IOI), VEGF (1VPF), MMP-2 (7XGJ), and MMP-9 (1L6J). The goal was to elucidate the molecular basis of the anticancer potential of these compounds. Overall, the docking results indicate that the quinoline scaffold exhibits robust and consistent binding affinities across multiple carcinogenic targets, often surpassing those of the reference drug 5-fluorouracil (5-FU).

Comparative Binding Affinity Analysis

While 5-FU displayed weaker binding energies (−4.1 to −6.1 kcal/mol), the synthesized derivatives demonstrated more favorable energies, ranging from −6.2 to −10.5 kcal/mol across all tested targets. QC-3 emerged as the most potent derivative, followed closely by QC-4 and QC-5. The planar heteroaromatic structure of quinoline derivatives facilitates π–π stacking, hydrogen bonding and hydrophobic interactions within protein active sites, accounting for the observed higher affinities. These results align with previous reports of quinoline-based inhibitors targeting apoptotic and angiogenic pathways [25,26].

Interactions with Apoptotic Regulators (Bcl-2, BAX, BAD)

Docking analyses revealed strong interactions of the quinoline derivatives with key residues essential for BH3-domain recognition, such as TYR180, GLU135, LYS20 and SER106 within anti-apoptotic proteins Bcl-2 and Bcl-xL (BAD complex). QC-3 and QC-4 exhibited the highest binding affinities (−8.3 to −8.4 kcal/mol), exceeding 5-FU by more than 3 kcal/mol. Similarly, interactions with BAX involved crucial residues GLN18, THR22, TRP158 and GLU159, suggesting stabilization of BAX in its active conformation to promote apoptosis. These dual interactions with both pro- and anti-apoptotic proteins indicate a broad regulatory potential, enhancing the therapeutic relevance of these quinoline derivatives [27–29].

Interaction with Tumor Suppressor Protein p53

Docking of the quinoline derivatives against the human and murine p53 core domains revealed favorable binding energies ranging from −6.3 to −6.9 kcal/mol, markedly superior to 5-fluorouracil (5-FU). Key residues, including SER99, ARG158, and ASP1205, which are critical for maintaining p53 structural stability and DNA-binding function, formed stable hydrogen bonds with the compounds. QC-3 and QC-1 exhibited the most favorable interaction geometries, suggesting potential as p53-reactivating agents capable of restoring tumor suppressor activity in cancer cells [30].

Potential Anti-Angiogenic and Anti-Metastatic Activity (VEGF, MMP-2, MMP-9)

The multi-target potential of the quinoline derivatives was further supported by docking against VEGF, MMP-2 and MMP-9. For VEGF, QC-3 and QC-5 displayed the strongest binding affinities, forming key hydrogen bonds with residues GLN22, CYS68 and ARG56, indicative of possible inhibition of angiogenic signaling pathways. Previous studies have similarly reported that quinoline scaffolds can modulate VEGF-mediated angiogenesis [31]. Docking against MMP-2 and MMP-9 revealed significant interactions with catalytic residues such as ALA140, ILE142, HIS121, GLU416 and LEU418, essential for metalloproteinase activity. QC-3 and QC-4 demonstrated optimal occupancy of the catalytic pocket, achieving binding energies as low as −10.5 kcal/mol. These findings suggest effective inhibition of extracellular matrix degradation, consistent with prior reports on quinoline-based anti-metastatic and MMP-targeting compounds [32,33].

Table 1(a-i): Binding affinities, hydrogen bonds and binding sites of QC-1 to QC-5 interacting with anticancer protein targets **a)**2BZW, **b)**1F16,**c)** 1G5M, **d)** 1VPF, **e)** 2IOI, **f)** 2OCJ, **g)** 5W62, **h)** 7XGJ **andi)** 1L6J compared with 5-FU as the control

a.

Compound	Binding Energy (kcal/mol)	Hydrogen bonding interaction of amino acid (distance) in (Å)	Amino acids in the binding site	Other amino acid interaction distances (Å)	Amino acids in the binding site
QC-1	-7.3	2.30	LYS20	4.87 4.44 4.22 4.40 4.61 3.71 4.30 4.50	LYS16 GLY148 ALA149 VAL152 GLU153 ASP156 LYS157
QC-2	-7.5	2.50 3.01 2.89	LYS20 SER106	4.50 3.66 4.93 4.14 4.43 4.39 2.48 5.14 3.80	LYS16 GLU98 ARG102 ALA149 VAL152 GLU153 ASP156
QC-3	-7.7	2.25 2.20	LYS20 SER106	4.69 5.20	LYS16 LYS20

				4.26	
				3.82	GLU98
				5.06	ARG102
				4.46	
				4.41	ALA149
				4.29	VAL152
				4.97	GLU153
				3.03	
				5.40	ASP156
				5.31	LYS157
				4.62	
		2.43	LYS20	4.66	LYS16
QC-4	-7.3	2.37	SER106	5.32	LYS20
				4.34	
				3.75	GLU98
				5.15	ARG102
				4.38	ALA149
				4.36	VAL152
				4.84	GLU153
				2.59	
				5.10	ASP156
				4.65	LYS157
		2.38	LYS20	4.72	LYS16
QC-5	-7.4	2.70	SER106	5.19	LYS20
				4.37	
				3.66	GLU98
				5.11	ARG102
				4.25	ALA149
				4.50	VAL152
				4.87	GLU153
				2.52	
				4.98	ASP156
				4.01	
				2.92	LYS16
5-FU	-4.6			3.38	GLN19
		-	-	4.99	LYS20
				3.29	GLU98
				2.25	

b.

Compound	Binding Energy (kcal/mol)	Hydrogen bonding interaction of amino acid (distance) in (Å)	Amino acids in the binding site	Other amino acid interaction distances (Å)	Amino acids in the binding site
QC-1	-7.8	3.53 3.44	GLU44	3.84 4.75 4.15 4.25 4.84 4.60	ALA35 ALA42 LUE45 VAL50
QC-2	-7.5	3.78	GLN32	3.74 5.19 4.55 4.20 5.28 5.28 4.78 4.64	ALA35 MET38 ALA42 LUE45 ALA46 VAL50
QC-3	-8.1	-	-	3.87 4.30 4.12 5.11 4.98 4.61	ALA35 ALA42 LUE45 VAL50
QC-4	-7.6	2.60 2.96 2.91 2.86	LYS21 THR56	5.01 5.07 4.91 4.92 5.35 4.81 4.97	ILE19 LUE25 PRO49 TRP158 LUE162
QC-5	-8.0			3.86 5.30 4.41	ALA35 MET38 ALA42

		--	--	4.26 5.10 4.83 4.70	 LUE45 VAL50
5-FU	-4.2	2.96 2.41 2.305	THR56 LUE25 GLN52	3.63 3.67	VAL50

c.

Compound	Binding Energy (kcal/mol)	Hydrogen bonding interaction of amino acid (distance) in (Å)	Amino acids in the binding site	Other amino acid interaction distances (Å)	Amino acids in the binding site
QC-1	-8.1	2.06	TYR180	4.22 4.45 4.49 5.15	ALA131 ARG139 VAL142 TYR180
QC-2	-7.6	1.98	TYR180	4.53 4.32 4.42 5.10	ALA131 ARG139 VAL142 TYR180
QC-3	-8.3	2.06	TYR180	4.18 5.47 4.51 4.46 5.11	ALA131 VAL134 ARG139 VAL142 TYR180
QC-4	-8.4	2.12 2.66	TYR180 GLU135	4.88 4.26 4.29 4.57	PHE130 ALA131 ARG139 VAL142
QC-5	-8.3	-	-	4.51 4.65 4.06	VAL36 ALA32
5-FU	-4.6	2.45 2.03	TRY9 ASN11	3.65	ASN182

d.

Compound	Binding Energy (kcal/mol) **1VPF**	Hydrogen bonding interaction of amino acid (distance) in (Å)	Amino acids in the binding site	Other amino acid interaction distances (Å)	Amino acids in the binding site

QC-1	-6.2	2.17 2.33 2.98 3.49	CYS68 CYS61 LUE66	4.14 5.09 4.25 5.33	ARG56 CYS60 VAL69
QC-2	-6.3	2.63 3.72 3.75	GLN22 PRO28	3.82 3.72	ARG23 HIS27
QC-3	-6.5	2.66	GLN22	5.15 4.83 4.89 4.36	TYR21 ARG23 TYR25 HIS27
QC-4	-6.2	2.21 4.97	ARG56 CYS68	4.67 4.18 4.04 5.16	ARG56 HIS99
QC-5	-6.3	2.29 2.50 1.95	ASP63 LUE66 CYS68	4.18 4.77 5.33 3.94 5.42 4.33	ARG56 CYS61 GLU67 VAL69
5-FU	-4.4	2.85 2.33 2.83 1.93 3.33	ARG82 GLN87 GLY88	5.08 5.13 3.97 3.90	ARG82 LYS84 HIS90

e.

Compound	Binding Energy (kcal/mol) 2I0I	Hydrogen bonding interaction of amino acid (distance) in (Å)	Amino acids in the binding site	Other amino acid interaction distances (Å)	Amino acids in the binding site
QC-1	-6.3	3.55 3.12 2.89	ARG1155 ASP1205	4.07 5.37 4.14 3.91 3.05 4.70	ARG1155 MET1157 LUE1203 ASP1205 ILE1251
		3.32	SER1212	3.24	ARG1155

QC-2	-6.5			4.78 4.74 4.17 4.82 3.74 5.05 5.39 3.94	ILE1159 LUE1203 GLU1204 ASP1205 GLU1255 LUE1261
QC-3	-6.6	3.21	ARG1155	3.64 3.93 3.88 2.61 5.21	MET1157 LUE1203 ASP1205 ILE1251
QC-4	-6.4	4.47 3.56 3.18	ARG1155 ASP1205	4.09 3.91 3.85 4.68 3.73 2.25 4.98	MET1157 LUE1203 ASP1205 ILE1251
QC-5	-6.4	2.89 3.85	ARG1171 VAL1169	3.60 3.76 4.41 3.27 4.77	ARG1171 VAL1169 GLU1204 PHE1209
5-FU	-4.1	2.76 2.06 3.33 2.72 2.31	TRY1160 VAL1169 ARG1171 GLY1241 GLY1242	3.11 3.30	GLU1168

f.

Compound	Binding Energy (kcal/mol)	Hydrogen bonding interaction of amino acid (distance) in (Å)	Amino acids in the binding site	Other amino acid interaction distances (Å)	Amino acids in the binding site
QC-1	-6.9	2.90 2.79 2.98	SER99 ARG158	3.38 3.58 4.38 3.98	ARG158 MET160

				4.92 3.65 4.19 4.89	ILE254 THR256 GLU258 ARG267
QC-2	-6.7	2.98 2.85 3.01	SER99 ARG158	3.51 3.33 4.36 3.99 4.99 3.67 4.18 4.93	ARG158 MET160 ILE254 THR256 GLU258 ARG267
QC-3	-6.9	3.00 2.90 2.85	SER99 ARG158	3.55 3.53 4.33 40.4 5.01 3.70 4.06	ARG158 MET160 ILE254 THR256 GLU258
QC-4	-6.5	3.03 3.00 2.83	SER99 ARG158	3.54 3.52 4.35 4.04 5.00 3.67 3.78	ARG158 MET160 ILE254 THR256 GLU258
QC-5	-6.8	3.00 2.91 2.90	SER99 ARG158	3.58 3.51 4.33 4.03 5.01 3.70 4.07	ARG158 MET160 ILE254 THR256 GLU258
5-FU	-4.5	2.24 3.05 3.59 3.49 2.23	SER99 ARG158 ARG267	4.95 4.51	ARG267

g.

Compound	Binding Energy (kcal/mol)	Hydrogen bonding interaction of amino acid (distance) in (Å)	Amino acids in the binding site	Other amino acid interaction distances (Å)	Amino acids in the binding site
QC-1	-7.9	2.56 2.97	GLN18 GLU159	4.00 4.01 3.84	LYS21 PHE25
QC-2	-7.7	2.77 2.14 2.25	GLN18 THR22	4.05 4.22 3.68 5.06	LYS21 PHE25 LYS57
QC-3	-8.4	2.67 2.16 2.67 2.62	GLN18 THR22 TRP158 GLU159	3.33 3.93 4.11 3.68 5.03	PRO13 LYS21 PHE25 LYS57
QC-4	-8.2	2.78 2.21 2.78 1.98	GLN18 THR22 TRP158 GLU159	5.10 3.49 3.98 4.29 3.67 5.17 3.31	PRO13 LYS21 PHE25 LYS57 GLY156
QC-5	-8.2	2.68 2.20 2.55 2.07	GLN18 THR22 TRP158 GLU159	3.84 4.07 3.89	LYS21 PHE25
5-FU	-4.5	2.11 2.09 2.01 3.43	PRO13 THR22 GLU159 TRP158	4.98 2.34	PRO13 GLN18

h.

Compound	Binding Energy (kcal/mol) 7XGJ	Hydrogen bonding interaction of amino acid (distance) in (Å)	Amino acids in the binding site	Other amino acid interaction distances (Å)	Amino acids in the binding site

		3.47	ALA140	5.15	LUE83
QC-1	-9.7	3.58	ILE142	4.96	
				4.61	
				5.17	LUE117
				5.97	HIS121
				3.46	
				5.79	HIS131
				5.13	LUE138
		3.73	ALA140	5.31	LUE83
QC-2	-9.0	3.63	ILE142	4.88	
				4.67	
				5.04	LUE117
				5.88	HIS121
				3.51	
				5.13	HIS131
				4.92	
				5.20	LUE138
		3.39	ALA140	5.18	LUE83
QC-3	-10.5	3.71	ILE142	4.64	
				5.02	
				5.12	LUE117
				3.47	HIS121
				5.84	HIS131
				5.16	LUE138
		3.01	ALA140	5.20	LUE83
QC-4	-9.7	3.57	ILE142	3.95	
				5.08	LUE117
				4.96	HIS121
				3.79	
				4.34	HIS125
				5.44	HIS131
				5.11	LUE138
				5.26	PHE149
		3.46	ALA140	5.47	LUE82
QC-5	-9.9	3.08	THR144	5.12	LUE83
				5.12	
				4.73	
				5.13	LUE117
				5.79	HIS121

				5.54 3.52 5.16 5.25 5.11	 HIS131 LUE138 ILE142
5-FU	-5.7	2.96 2.45 2.36	ALA140 ILE142 THR144	3.25	LUE117

i.

Compound	Binding Energy (kcal/mol)	Hydrogen bonding interaction of amino acid (distance) in (Å)	Amino acids in the binding site	Other amino acid interaction distances (Å)	Amino acids in the binding site
QC-1	-8.1	3.41 3.80 3.49 2.90	GLU130 THR336 ALA333	5.42 3.95 3.69 3.68 4.60	PRO133 PRO219 ARG332
QC-2	-8.9	1.70 2.86 3.41	GLU416 HIS432 PRO430	4.93 3.82 5.44 3.81 3.23 2.69	LEU397 LEU418 ARG424 THR426
QC-3	-9.2	1.78	GLU416	3.92 4.95	LUE418 LUE397
QC-4	-9.2	1.62 3.53	GLU416 ALA417	4.96 3.75 4.21 3.75	LUE397 VAL398 HIS401 LUE418
QC-5	-8.9	1.74	GLU416	5.02 3.92	LUE397 LUE418
5-FU	-6.1	2.88 2.23 2.33	VAL217 THR331 ALA333	-	-

a

Compounds	Protein-ligand interaction	2D- structure
QC-1		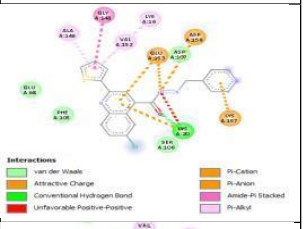
QC-2	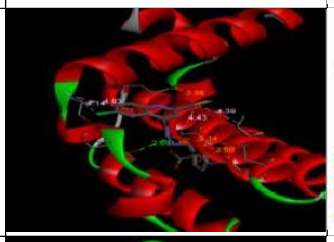	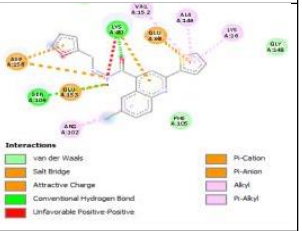
QC-3		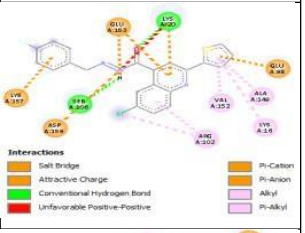
QC-4	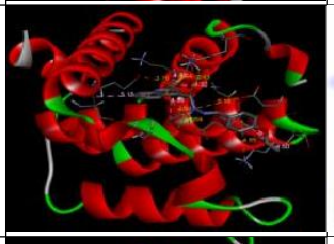	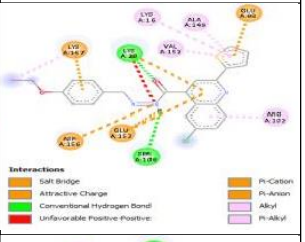
QC-5		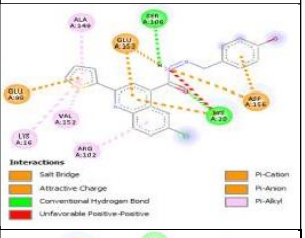
5-FU	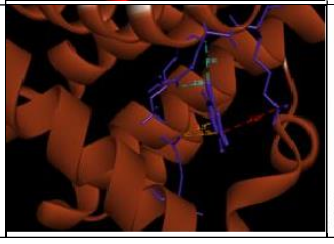	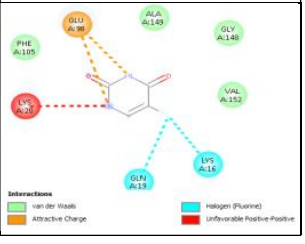

b

Protein-ligand interaction	2D- structure
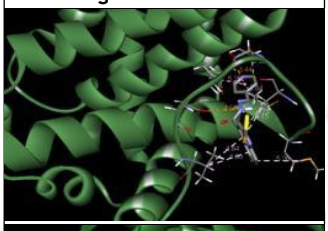	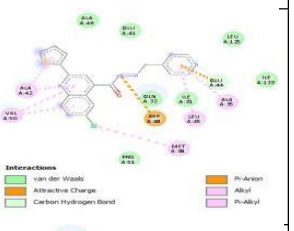
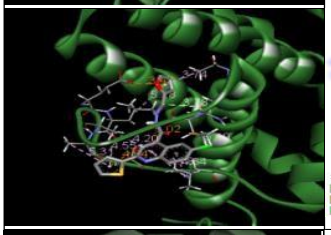	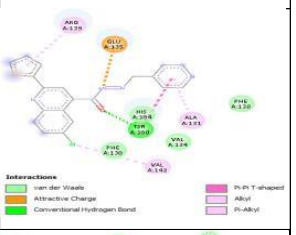
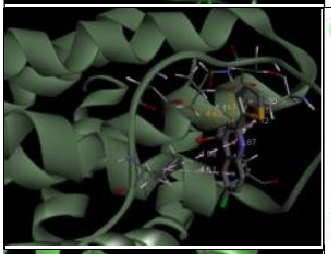	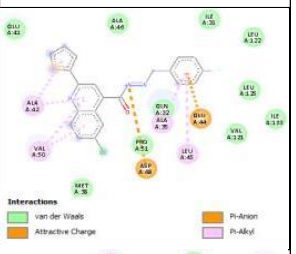
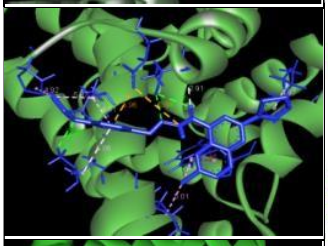	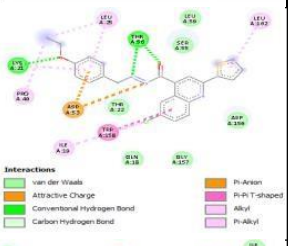
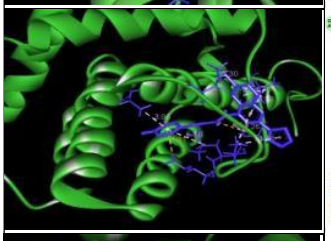	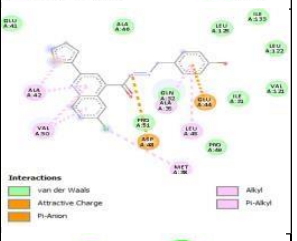
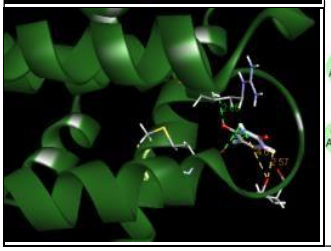	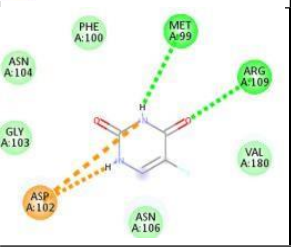

c			d	
Compounds	Protein-ligand interaction	2D- structure	Protein-ligand interaction	2D- structure
QC-1	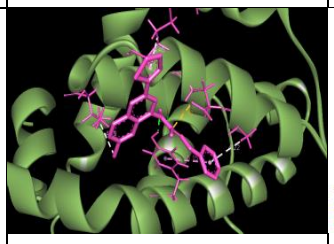	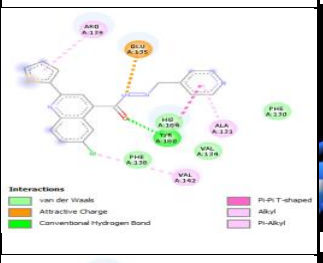	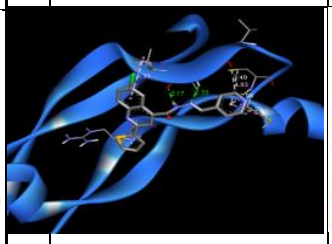	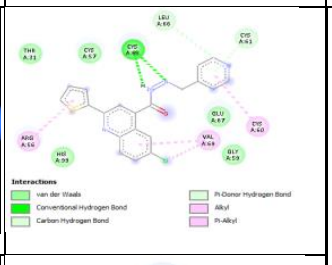
QC-2	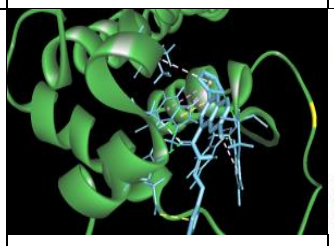	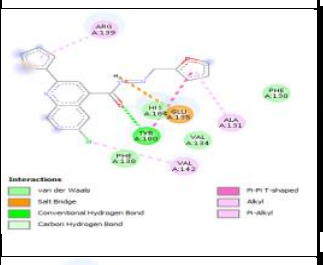	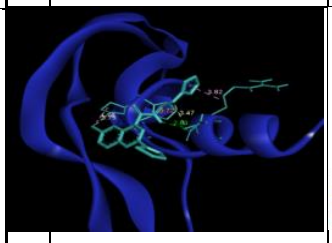	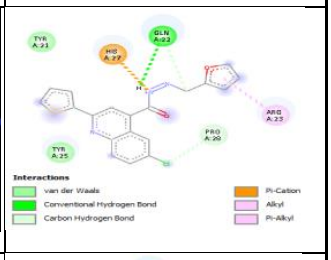
QC-3	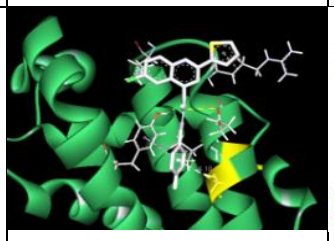	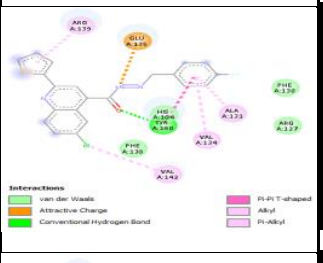	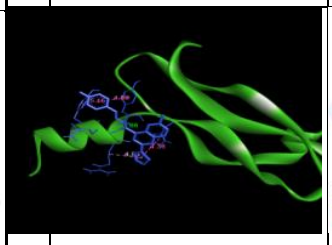	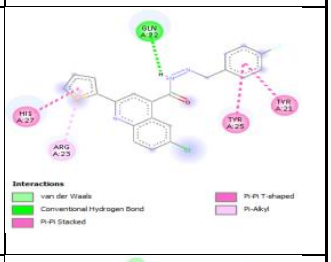
QC-4	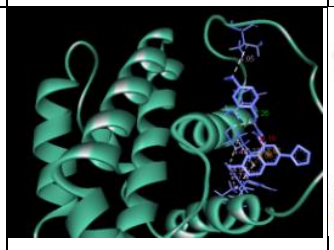	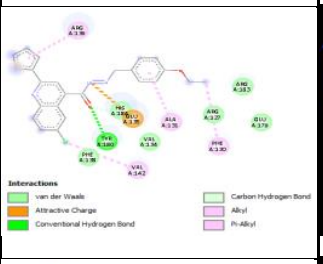	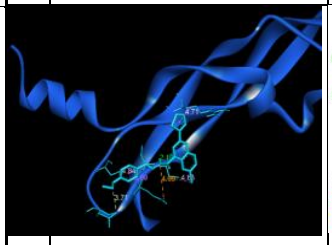	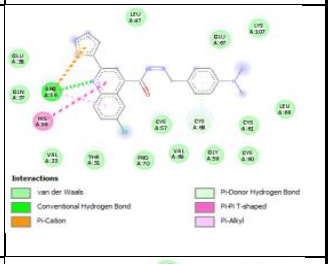
QC-5	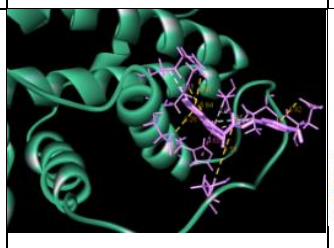	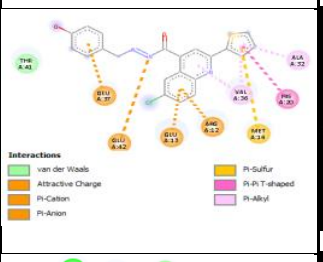	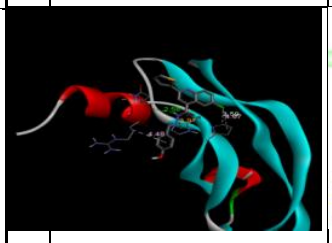	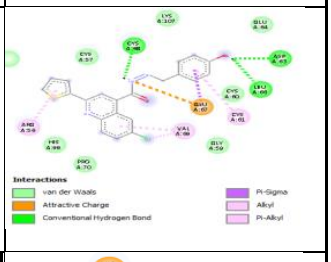
5-FU	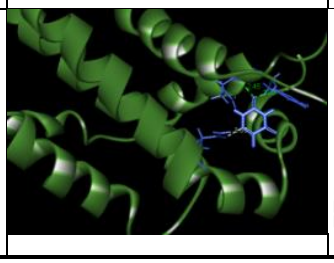	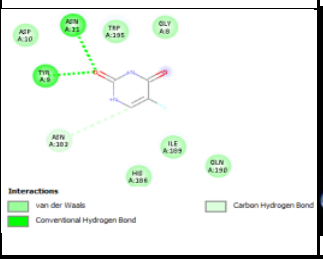	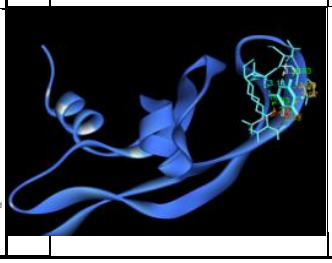	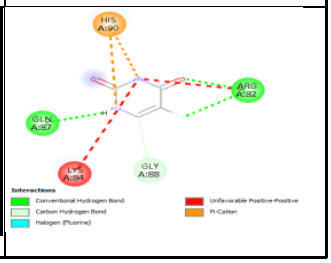

e			f	
Compounds	Protein-ligand interaction	2D- structure	Protein-ligand interaction	2D- structure
QC-1	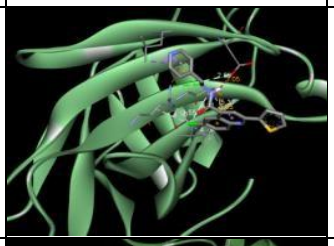	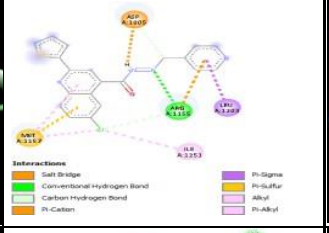	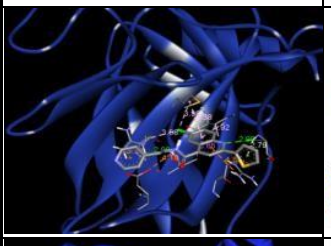	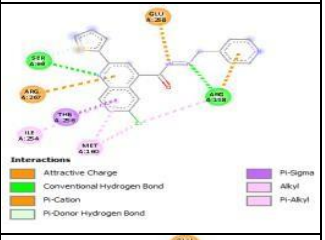
QC-2	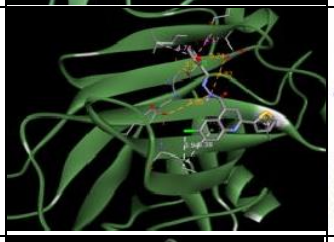	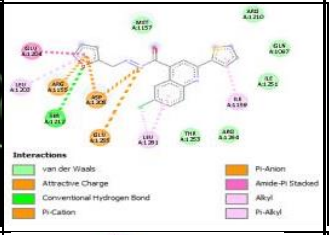		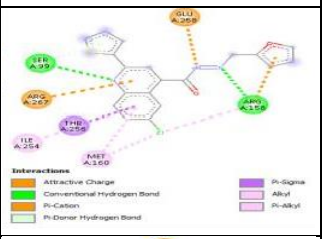
QC-3		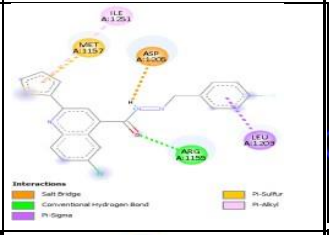	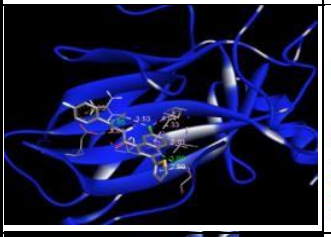	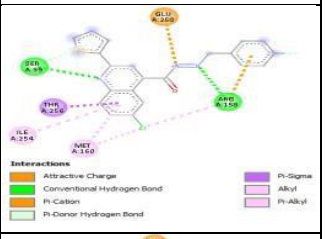
QC-4		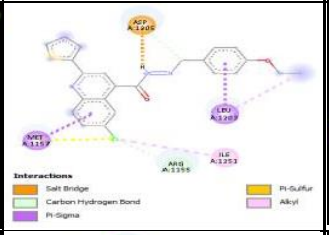	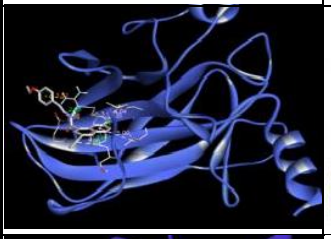	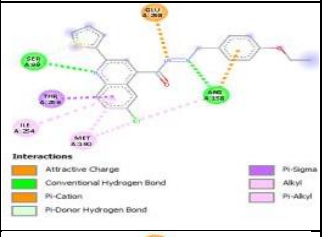
QC-5	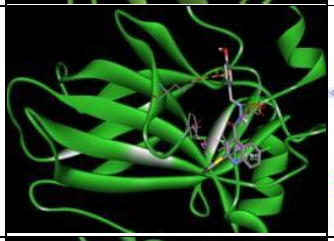	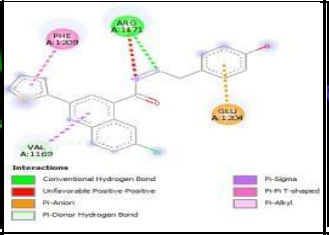	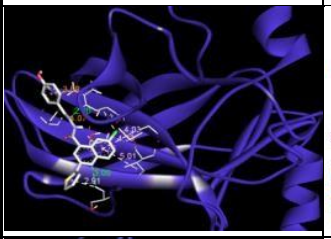	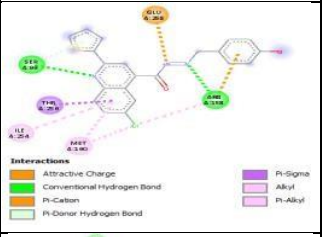
5-FU	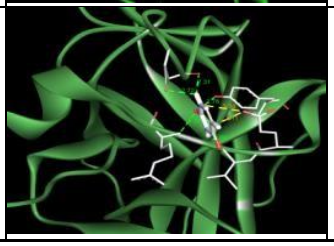	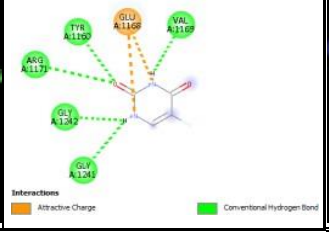	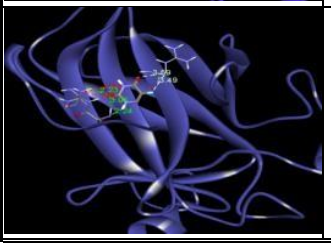	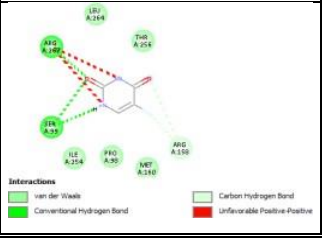

g			h	
Compounds	Protein-ligand interaction	2D- structure	Protein-ligand interaction	2D- structure
QC-1	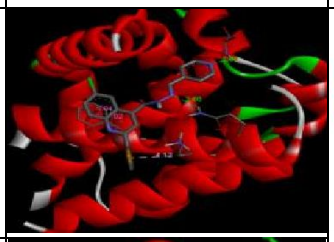	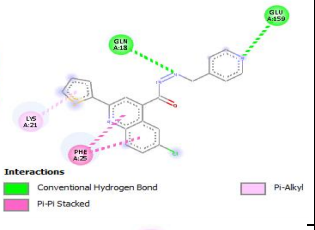	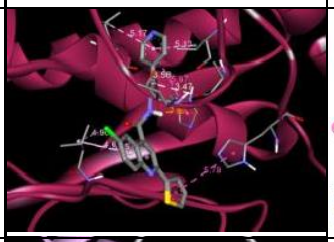	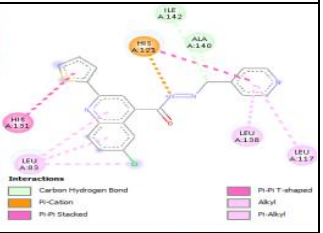
QC-2	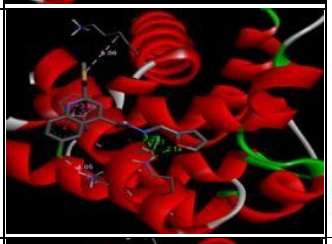	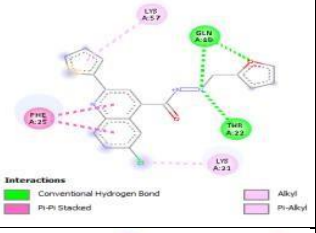	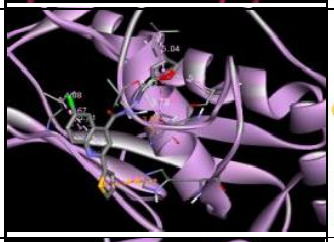	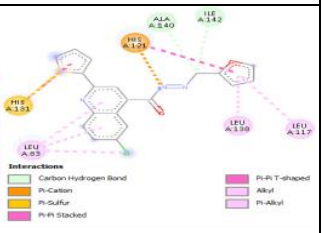
QC-3	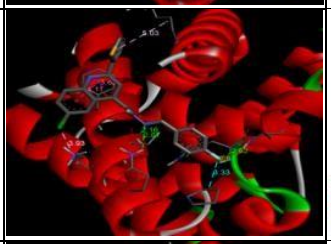	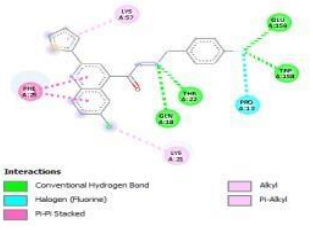	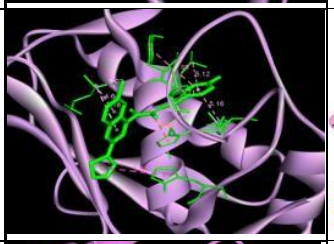	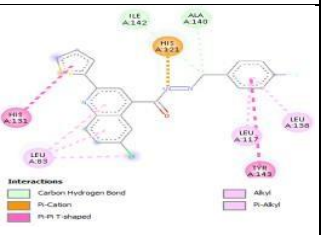
QC-4		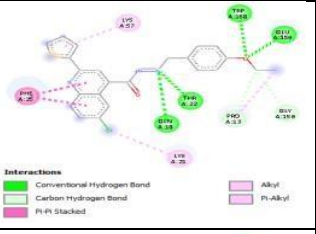	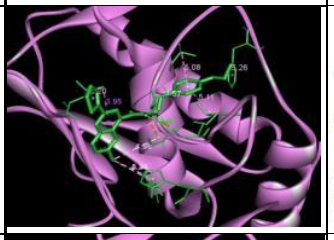	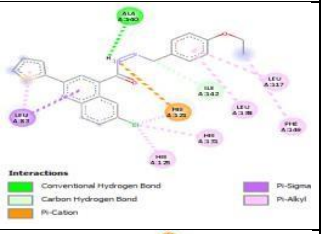
QC-5	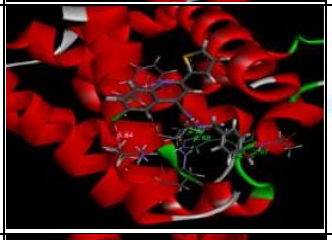	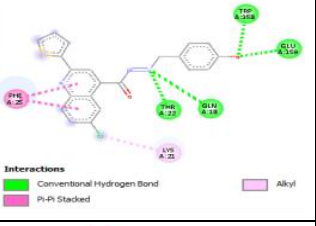	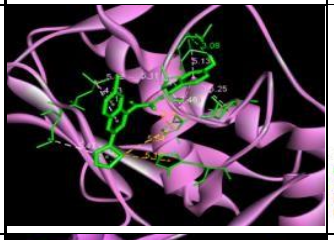	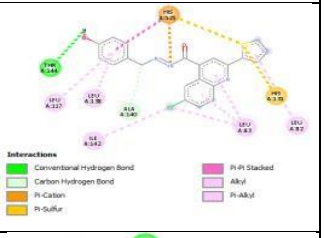
5-FU	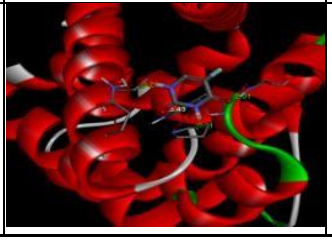	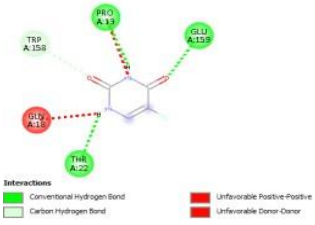	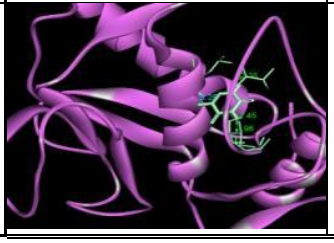	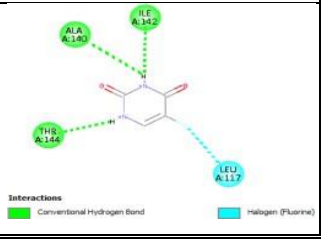

i.

Compounds	Protein-ligand interaction	2D- structure
QC-1	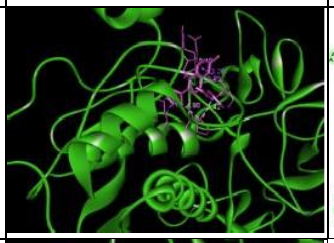	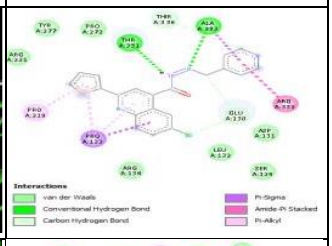
QC-2	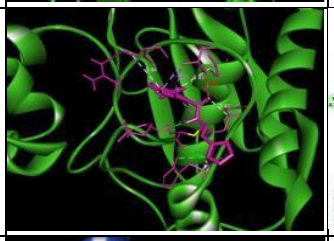	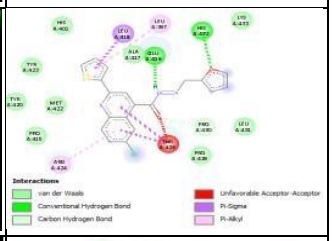
QC-3	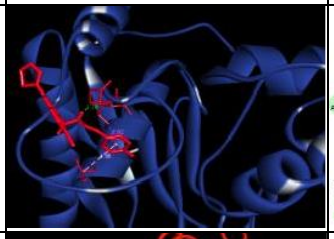	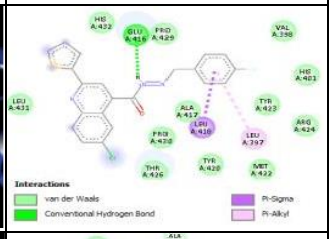
QC-4		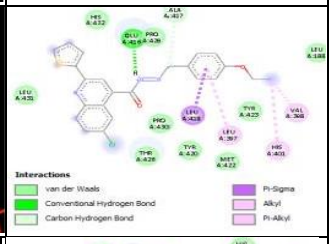
QC-5		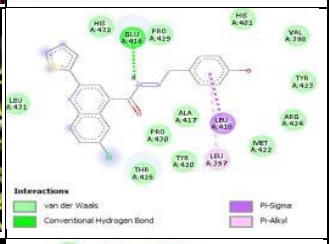
5-FU	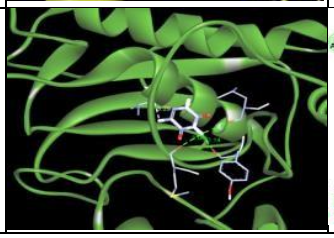	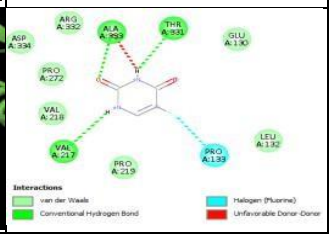

Figure 2 a-i : The binding interactions between the cancer causing proteins; a) 2BZW, b) 1F16, c) 1G5M, d) 1VPF, e) 2IOI, f) 2OCJ, g) 5W62, h) 7XGJ and i) 1L6J with QC and 5-FU used as reference. The general binding pocket design for above proteins that accommodates the quinoline derivatives appears by the ribbon. The interactions, including as hydrophobic contacts, hydrogen bonds and other non-covalent interactions involved in ligand binding, are shown in the 2D interaction diagrams

5. MOLECULAR DYNAMIC ANALYSIS

Protein Backbone RMSD

Figure 3 illustrates the root mean square deviation (RMSD) of protein Cα atoms over a 100 ns molecular dynamics simulation, calculated relative to the initial minimized structure. The RMSD values (y-axis, nm) initially start at approximately 0.2 nm and gradually increase during the early phase of the simulation. Within the first 20 ns, a steady rise in RMSD is observed, reflecting initial structural relaxation and adaptation of the protein to the bound ligand. Between 20 and 60 ns, a more pronounced increase in RMSD is evident, reaching approximately 0.6 nm, indicating notable conformational rearrangements. Beyond 60 ns, the RMSD stabilizes around 0.6 nm with only minor fluctuations, suggesting that the protein attains a new equilibrium conformation. Overall, the RMSD profile indicates acceptable structural stability of the protein–ligand complex after initial conformational adjustments.

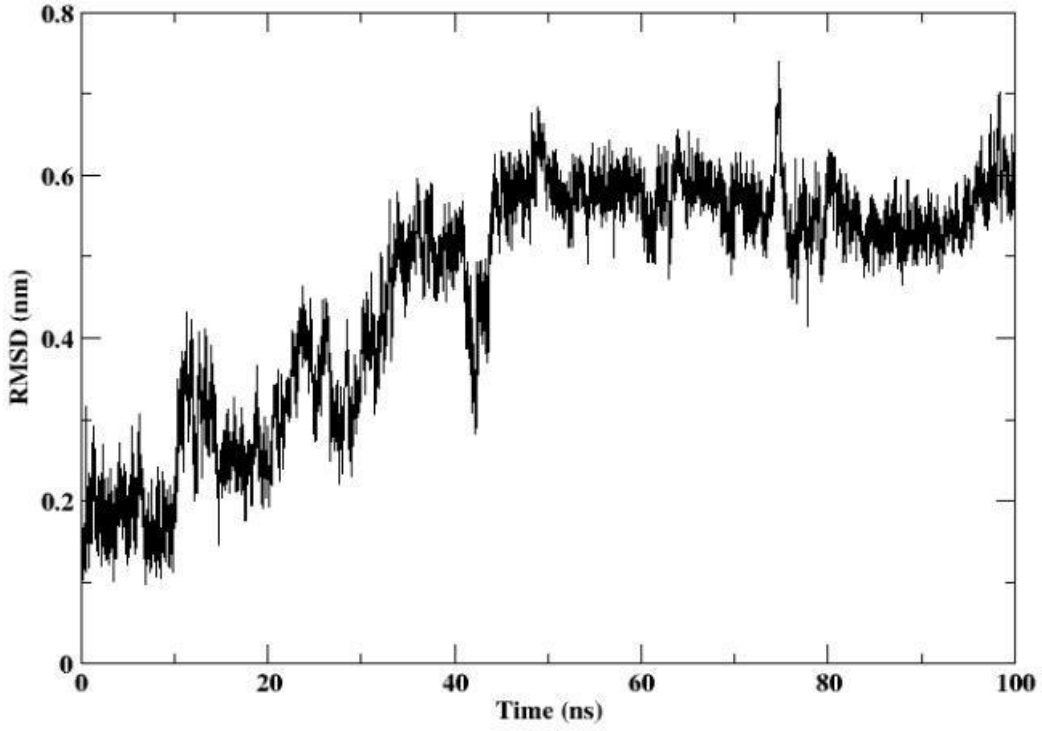

Figure 3. RMSD of protein Cα-atoms aligned over the initial structure for VEGF protein.

Ligand RMSD

Figure 4 depicts the RMSD of the ligand during the 100 ns simulation, calculated relative to its initial bound conformation. For the first 60 ns, the ligand RMSD remains low and stable (approximately 1.0 nm), indicating minimal conformational deviation and stable binding within the protein pocket. A sharp increase in RMSD is observed between 60 and 80 ns, with values rising to ~10 nm. This abrupt change suggests a major conformational rearrangement or partial dissociation of the ligand from the binding site. After 80 ns, the RMSD fluctuates at elevated values, indicating that the ligand adopts a new conformation and does not revert to its original binding pose, while continuing to undergo minor dynamic adjustments.

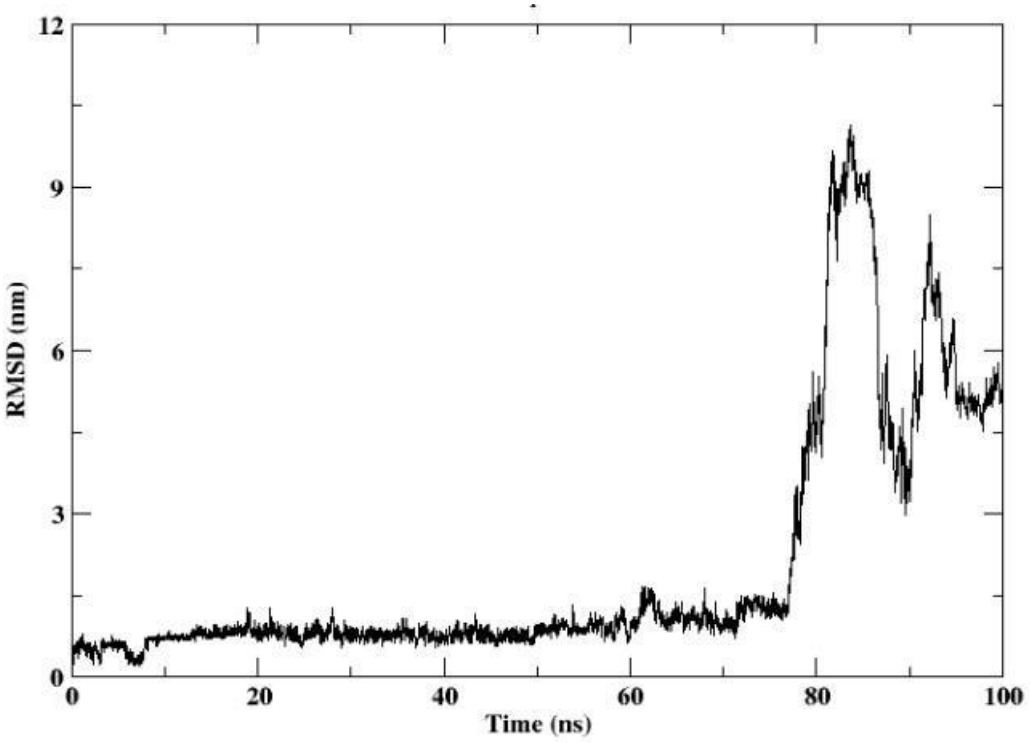

Figure 4. RMSD of the ligand aligned over the initial structure for the 100 ns simulation.

Conformational Changes During Simulation

Figure 5 presents snapshots of ligand conformational changes within the protein binding site at selected time points (0, 75, 76, 77 and 78 ns). Up to 75 ns, the ligand remains stably positioned within the binding pocket, consistent with the low RMSD values observed earlier. At 75 ns, noticeable displacement of the ligand is observed, marking the onset of significant conformational changes. At 76 and 77 ns, the ligand undergoes progressive repositioning within the binding pocket, indicating a transitional phase characterized by dynamic protein-ligand interactions. By 78 ns, the ligand is observed moving out of the binding site, consistent with the sharp increase in ligand RMSD. These observations highlight the dynamic nature of the protein-ligand interaction and suggest a time-dependent binding adaptability, potentially associated with conformational searching for an alternative stable state (Figure 5).

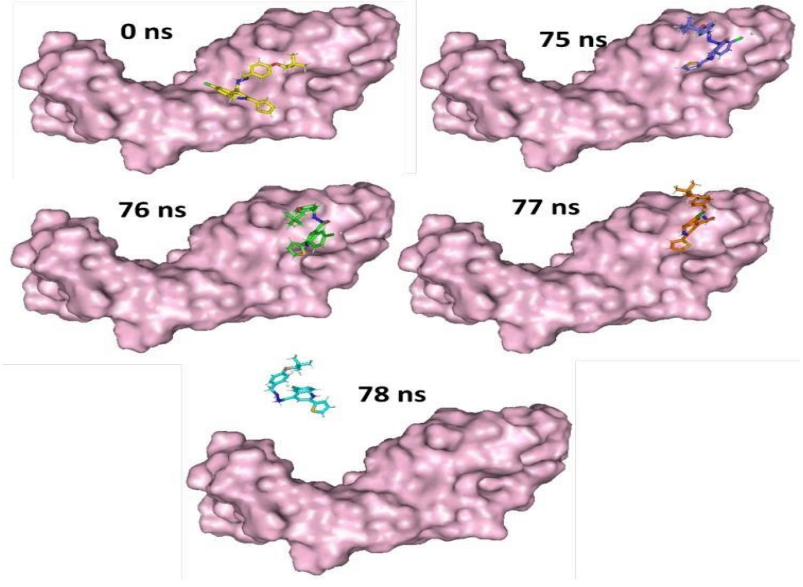

Figure 5. Confirmation of the ligand when bound to the protein at 0 ns, 75 ns, 76 ns, 77 ns, and 78 ns

Root Mean Square Fluctuation (RMSF) Analysis

Figure 6 illustrates the root mean square fluctuation (RMSF) of the protein residues in the protein–ligand complex over a 100 ns molecular dynamics simulation. RMSF values, plotted in nanometers (nm) on the y-axis against residue numbers on the x-axis, represent the flexibility and dynamic behavior of individual amino acid residues throughout the simulation. Higher RMSF values are observed at the N-terminal region, with fluctuations reaching approximately 1.5 nm, indicating greater flexibility in this segment of the protein. This increased mobility is commonly associated with terminal regions, which are typically less structurally constrained. Following this region, RMSF values decrease sharply and remain relatively stable across the central portion of the protein, with fluctuations predominantly below 0.3 nm. This low level of fluctuation suggests that the core residues of the protein maintain structural rigidity and stability upon ligand binding. Toward the C-terminal region, a modest increase in RMSF is observed, reflecting slightly enhanced flexibility; however, these fluctuations are considerably lower than those observed at the N-terminus. Overall, the RMSF profile indicates a stable protein–ligand complex, with localized flexibility confined mainly to terminal regions, while the binding-site residues remain structurally stable during the simulation.

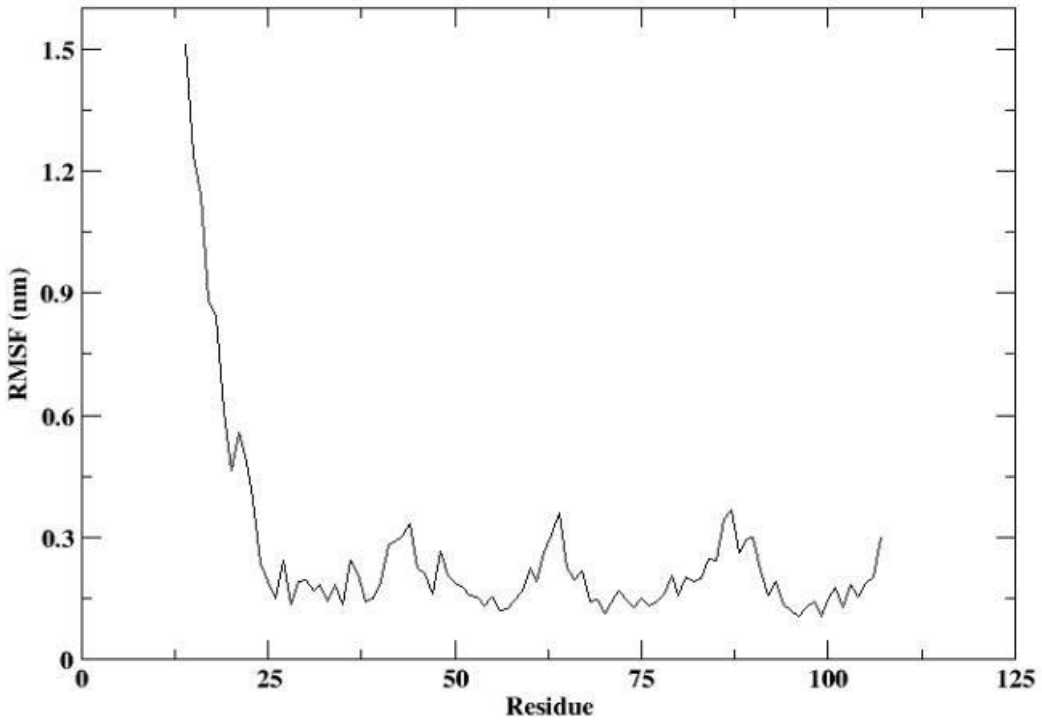

Figure 6. RMSF of the protein when bound to the ligand for the 100 ns simulation.

Solvent-Accessible Surface Area (SASA) Analysis

Figure 7 illustrates the solvent-accessible surface area (SASA) of the protein–ligand complex over a 100 ns molecular dynamics simulation. SASA values fluctuate between approximately 66 nm^2 and 78 nm^2 throughout the simulation, reflecting dynamic changes in solvent exposure as the protein undergoes conformational adjustments. The observed fluctuations indicate continuous modulation of protein–solvent interactions, likely driven by structural rearrangements of surface-exposed residues and ligand-induced conformational flexibility. Importantly, the absence of a consistent upward or downward trend suggests that the protein does not undergo sustained global expansion or contraction during the simulation. Instead, the complex appears to sample multiple conformational states, each characterized by varying degrees of solvent accessibility.

The recurring peaks and troughs in the SASA profile may correspond to transient opening and closing of structural elements or localized rearrangements near the binding site, which alternately increase and decrease solvent exposure. Such behaviour is characteristic of a dynamically stable protein–ligand system rather than structural destabilization. Overall, the SASA analysis supports the structural integrity of the protein–ligand complex while highlighting its dynamic nature. The observed variability in solvent exposure is consistent with ligand-induced conformational flexibility and reversible binding-associated motions occurring throughout the simulation.

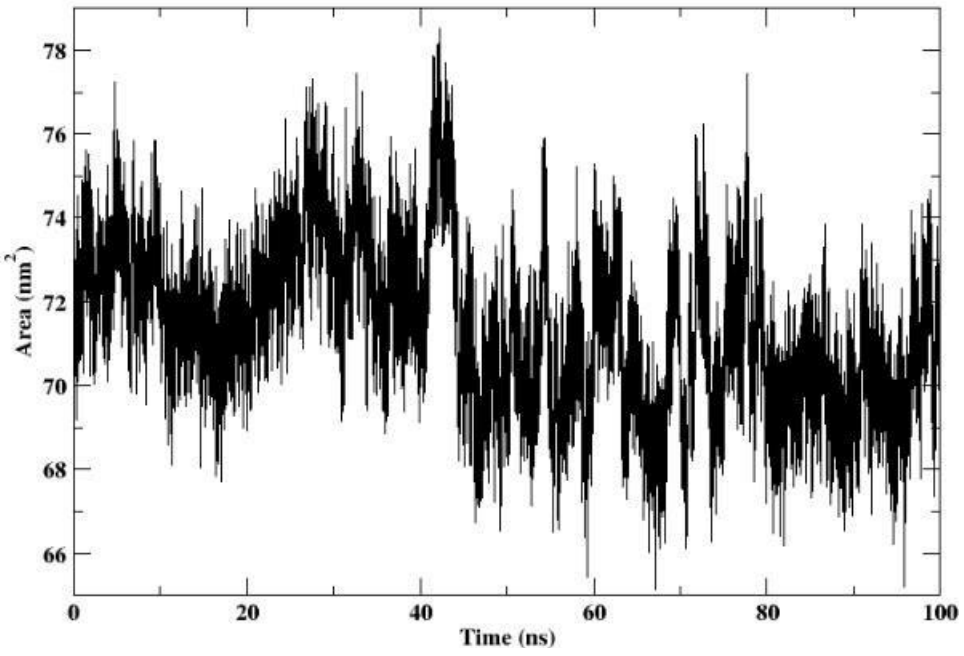

Figure 7. SASA of the protein when bound to the ligand for the 100 ns simulation.

Radius of Gyration (Rg) Analysis

Figure 8 presents the radius of gyration (Rg) of the protein-ligand complex over the course of a 100 ns molecular dynamics simulation. The Rg, expressed in nanometers (nm), reflects the overall compactness and structural distribution of the protein. During the initial phase of the simulation (0–40 ns), the Rg fluctuates around approximately 1.8 nm, indicating that the protein-ligand complex maintains a relatively stable and compact conformation, albeit with minor fluctuations reflecting inherent structural flexibility. Around 40 ns, a noticeable decrease in Rg is observed, with values dropping to approximately 1.7 nm. This reduction suggests a transition toward a more compact structural state, potentially driven by ligand-induced stabilization or conformational tightening of the protein.

Following this transition, from 40 to 100 ns, the Rg remains relatively stable at the lower value, with only minor fluctuations. This stability indicates that the protein retains its condensed conformation throughout the latter phase of the simulation, supporting the formation of a stable protein-ligand complex. Overall, the Rg profile demonstrates a ligand-associated compaction event during the simulation, followed by sustained structural stability. These findings, together with RMSD and SASA analyses, suggest that the protein undergoes controlled conformational adjustments before reaching a stable and compact state.

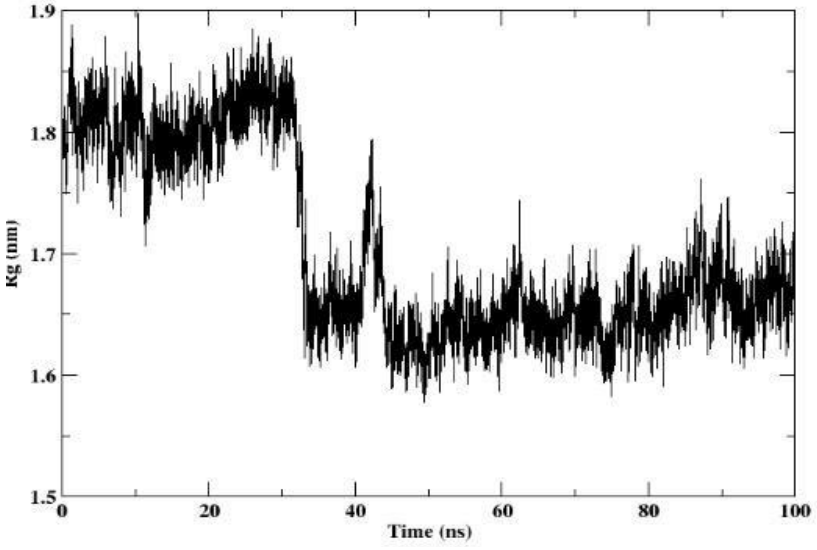

Figure 8. Radius of gyration of protein complex with the ligand for 100 ns of simulation.

Hydrogen Bond Analysis

Figure 9 depicts the number of hydrogen bonds formed between the protein and ligand during the 100 ns molecular dynamics simulation. The x-axis represents simulation time (ns), while the y-axis indicates the number of hydrogen bonds, ranging from 0 to 5. During the initial phase of the simulation (0–20 ns), the number of hydrogen bonds fluctuates between 1 and 3, indicating an early adjustment period as the protein–ligand complex establishes stabilizing interactions. From 20 to 45 ns, hydrogen bonding becomes more stable, with consistently 2–3 hydrogen bonds maintained and minimal fluctuations. This period reflects a relatively stable binding phase, supported by persistent intermolecular interactions.

Between 45 and 60 ns, a noticeable reduction in hydrogen bonds is observed, with intermittent drops to zero. This disruption suggests transient destabilization of the protein–ligand interactions, potentially due to conformational rearrangements or partial ligand displacement. In the final phase of the simulation (60–100 ns), hydrogen bond numbers fluctuate between 1 and 3, indicating dynamic binding behavior characterized by alternating periods of stabilization and rearrangement. Overall, the hydrogen bond profile highlights the dynamic nature of the protein–ligand interaction. Periods of stable hydrogen bonding are interspersed with transient disruptions, reflecting conformational adaptability of the complex during the simulation. These findings are consistent with RMSD, SASA, and Rg analyses, supporting a binding mechanism involving dynamic yet reversible interactions.

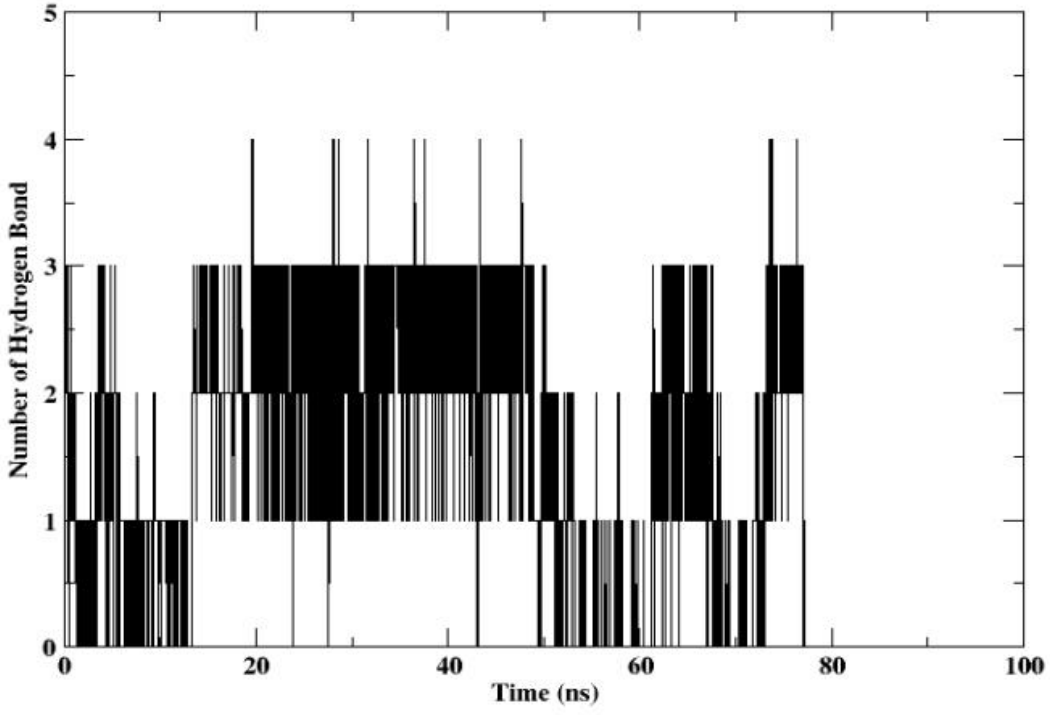

Figure 9. A hydrogen bond formed between the protein and the ligand for the 100 ns simulation.

Free Energy Landscape Analysis

Figure 10 presents the free energy landscape (FEL) of the protein–ligand complex obtained from a 100 ns molecular dynamics simulation. The FEL is represented using a two-dimensional contour plot (left) and a corresponding three-dimensional surface plot (right), constructed based on the first two principal components (PC1 and PC2), which describe the dominant collective motions of the system. The color scale denotes the relative free energy (ΔG, arbitrary units), with red regions indicating low-energy, stable conformations and blue regions representing high-energy, less favorable states.

The contour plot illustrates the distribution of conformational states sampled during the simulation within the PC1–PC2 space. Distinct low-energy basins are observed, corresponding to energetically favorable and stable conformations of the protein–ligand complex. Notably, the presence of two major low-energy minima suggests that the complex can adopt at least two stable conformational states during the simulation. In contrast, the scattered high-energy regions (blue areas) represent unstable or transient conformations that are sampled less frequently.

The three-dimensional surface plot provides a more comprehensive visualization of the FEL, clearly depicting the depth and topology of the energy minima. The deep valleys correspond to the stable conformations identified in the contour plot, while the elevated peaks represent energetically unfavorable states. The pronounced depth of the energy wells indicates strong stabilization of specific conformations, whereas the energy barriers separating these minima suggest that transitions between different stable states require overcoming significant energetic constraints. Overall, the FEL analysis demonstrates that the protein–ligand complex explores a broad

conformational space but preferentially occupies a limited number of low-energy states. This behavior reflects a dynamically stable binding mechanism, consistent with the RMSD, hydrogen bond, and radius of gyration analyses, and supports the formation of energetically favorable and persistent protein–ligand interactions throughout the simulation.

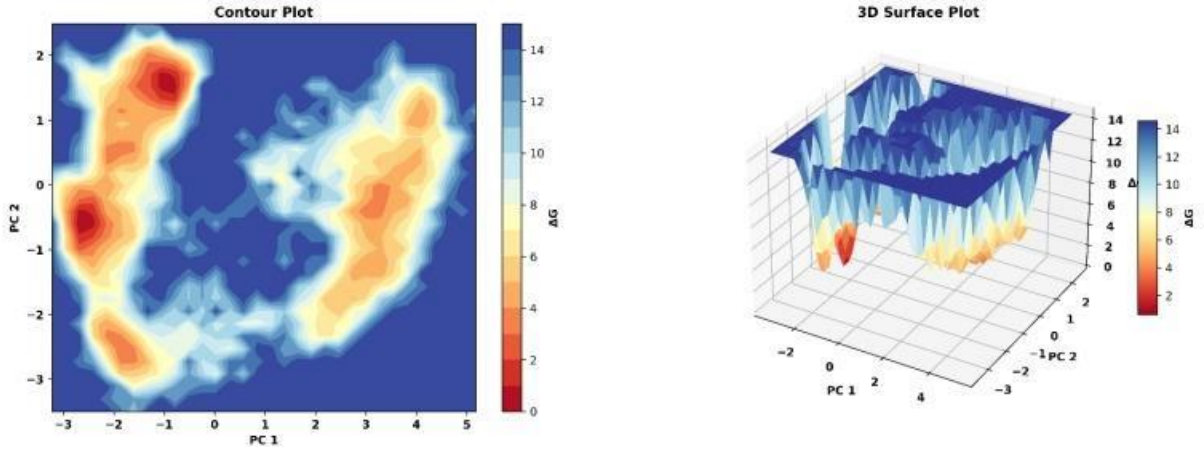

Figure 10. Free energy landscape of the protein when bound to the ligand for the 100 ns simulation.

Binding Free Energy Analysis

Figure 11 illustrates the binding free energy components of the protein–ligand complex calculated using the MM/GBSA approach over a 100 ns molecular dynamics simulation. The van der Waals energy (ΔE_VDWAALS = −15.06 kcal/mol) contributes moderately to complex stabilization, while electrostatic interactions (ΔE_EEL = −197.43 kcal/mol) play a dominant role in driving ligand binding. In contrast, the polar solvation energy (ΔE_GB = +197.84 kcal/mol) exerts a strong destabilizing effect, reflecting the energetic cost associated with desolvation upon complex formation. The nonpolar solvation term (ΔE_SURF = −2.57 kcal/mol) provides a minor stabilizing contribution, consistent with hydrophobic interactions at the binding interface. The total gas-phase energy (ΔG_GAS = −212.49 kcal/mol) indicates highly favorable protein–ligand interactions dominated by electrostatic and van der Waals forces. However, this favorable contribution is largely counterbalanced by the positive total solvation energy (ΔG_SOLV = +195.27 kcal/mol), primarily due to the polar solvation component. Consequently, the overall binding free energy (ΔG_BIND = −17.23 kcal/mol) remains modestly negative, confirming that ligand binding is energetically favorable but not excessively strong. Overall, the binding free energy profile reveals a balance between strong gas-phase interactions and unfavorable solvation effects, a characteristic feature of many protein–ligand systems. These results support stable yet dynamic binding, consistent with the molecular docking and molecular dynamics analyses.

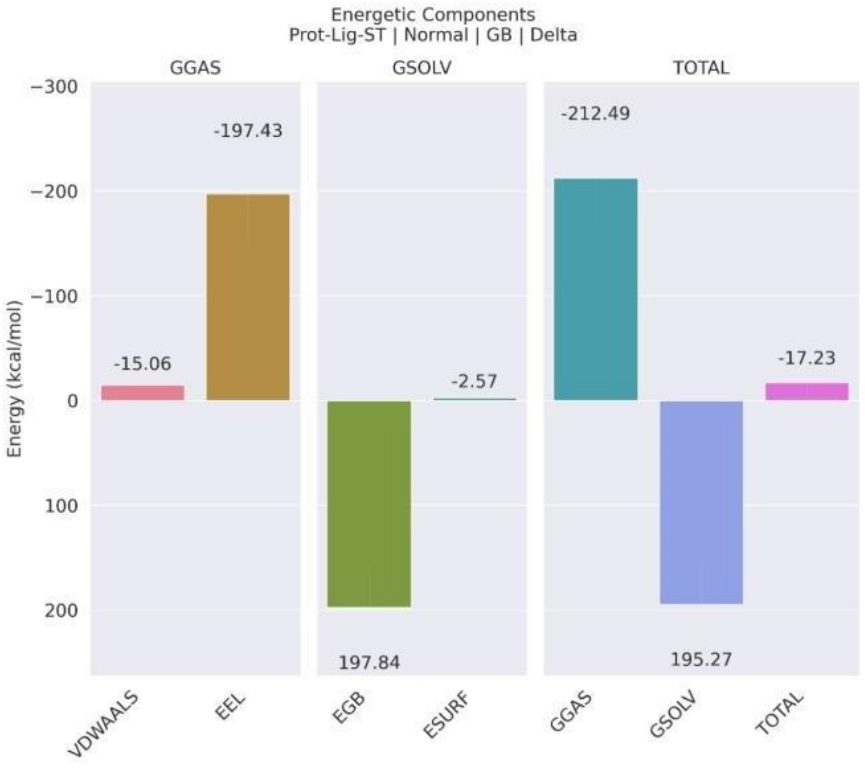

Figure 11. The binding free energy of the protein when bound to the ligand for the 100 ns simulation.

6. DISCUSSION

The present study provides a comprehensive evaluation of the antioxidant and anticancer potential of newly synthesized quinoline derivatives (QC-1 to QC-5) by integrating *in vitro* radical scavenging assays with *in silico* molecular docking analyses. Collectively, the findings highlight the quinoline scaffold as a versatile and promising pharmacophore for the development of multifunctional therapeutic agents with combined redox-modulating and anticancer properties. In agreement with earlier reports on quinoline-based antioxidants [23,24], both DPPH and ABTS assays demonstrated a clear concentration-dependent radical scavenging activity for all synthesized derivatives. These antioxidant effects are primarily governed by hydrogen atom transfer and electron transfer mechanisms, which are strongly influenced by the nature and electronic distribution of substituents on the quinoline nucleus. Notably, QC-1 and QC-4 exhibited superior DPPH scavenging activity, whereas QC-2 and QC-4 performed more effectively in the ABTS assay. This divergence likely reflects the mechanistic differences between the two assays, as DPPH predominantly measures hydrogen atom transfer, while ABTS accommodates both hydrogen atom and single-electron transfer processes [36]. The enhanced ABTS activity of QC-2 and QC-4 suggests greater electron delocalization, plausibly arising from extended π-conjugation and electron-donating substituents. Importantly, excessive antioxidant potency is not always advantageous in anticancer therapy, as tightly regulated redox modulation—rather than complete radical suppression—can promote selective cytotoxicity in cancer cells [34]. In this context, the moderate yet significant antioxidant activity observed for the quinoline derivatives is biologically meaningful and supports their potential therapeutic relevance.

Molecular docking studies further provided mechanistic insights into the anticancer potential of these compounds by revealing strong and consistent interactions with multiple cancer-associated molecular targets, including apoptosis regulators (BAX, Bcl-2, BAD), tumor suppressor p53, angiogenesis-related VEGF and metastasis-associated MMP-2 and MMP-9. Notably, compounds displaying superior antioxidant performance—particularly QC-3 and QC-4—also exhibited the most favorable binding affinities and interaction profiles across several targets, suggesting a convergence of redox-modulating and anticancer mechanisms. Among the evaluated derivatives, QC-3 emerged as the most potent multitarget ligand, exhibiting strong binding affinities toward BAX, Bcl-2, MMP-2 and MMP-9. Its extended aromatic framework and the presence of multiple hydrogen bond donors and acceptors enabled stable interactions with key residues such as GLU135, TYR180, HIS131 and GLU416. These interactions are critically involved in the regulation of apoptotic signaling, extracellular matrix degradation, and tumor invasiveness, as previously reported [35]. Similarly, QC-4 demonstrated pronounced interactions with anti-apoptotic Bcl-2 and angiogenesis-related VEGF, indicating its potential role in enhancing apoptotic sensitivity while suppressing tumor vascularization. The ability of quinoline derivatives to engage both polar residues and hydrophobic binding pockets underscores their structural adaptability and pharmacological versatility.

The observed convergence of antioxidant and anticancer activities aligns with growing evidence that redox regulation plays a central role in cancer progression and therapeutic response [34,36]. Compounds capable of modulating intracellular redox balance may selectively sensitize cancer cells to apoptosis while minimizing damage to normal cells. In this regard, QC-2, QC-3 and QC-4 appear particularly promising, as their dual functionality—efficient radical scavenging combined with strong interactions with apoptosis- and metastasis-related proteins—suggests a synergistic mechanism of action. Finally, the consistently superior docking performance of these quinoline derivatives compared to the reference drug 5-fluorouracil highlights their potential as next-generation anticancer scaffolds. Their ability to engage multiple molecular targets is especially advantageous for addressing tumor heterogeneity and overcoming drug resistance, reinforcing the therapeutic promise of the quinoline framework.

7. CONCLUSION

Based on integrated experimental and computational investigations, the present study demonstrates that the synthesized quinoline derivatives (QC) possess significant antioxidant and anticancer potential. The DPPH and ABTS assays confirmed a clear dose-dependent radical scavenging activity, with QC-1, QC-2 and QC-4 exhibiting superior antioxidant performance, highlighting the critical role of electron-donating substituents in enhancing redox activity. Molecular docking and simulation studies further revealed strong and sustained interactions of the quinoline derivatives—particularly QC-3 and QC-4—with key cancer-related targets, including Bcl-2, BAX, p53, VEGF, MMP-2 and MMP-9. These findings support a multitarget mechanism involving apoptosis induction, angiogenesis inhibition, and suppression of metastatic pathways. Collectively, the results provide compelling evidence for the potential of quinoline-based scaffolds as multifunctional anticancer agents and warrant further *in vitro* and *in vivo* validation to advance their therapeutic development.

Acknowledgments

The authors gratefully acknowledge the Kuvempu University administration, Shivamogga, Karnataka, India, for providing the necessary facilities to carry out this research. The authors also thank the Molecular Biomedicine Laboratory, Department of Biotechnology, Sahyadri Science College, Shivamogga, Karnataka, India, for their technical support.

Funding

This research received no specific grant from any funding agency in the public, commercial, or not-for-profit sectors.

Competing Interests

The authors declare that they have no competing interests.

8. REFERENCES

1. Kushwaha P. Quinoline as a Privileged Structure: A Recent Update on Synthesis and Biological Activities. Curr Top Med Chem. 2024;24(27):2377-2419. doi: 10.2174/0115680266314303240830074056. PMID: 39313876
2. Hernández-Ayala LF, Guzmán-López EG, Galano A. Quinoline Derivatives: Promising Antioxidants with Neuroprotective Potential. Antioxidants (Basel). 2023 Oct 12;12(10):1853. doi: 10.3390/antiox12101853. PMID: 37891932; PMCID: PMC10604020
3. Ajani OO, Iyaye KT, Ademosun OT. Recent advances in chemistry and therapeutic potential of functionalized quinoline motifs - a review. RSC Adv. 2022 Jun 24;12(29):18594-18614. doi: 10.1039/d2ra02896d. PMID: 35873320; PMCID: PMC9231466.
4. Abdelmegeed H, Abdel Ghany LM, Youssef A, El-Etrawy AS, Ryad N. Exploring the antitumor potential of novel quinoline derivatives *via* tubulin polymerization inhibition in breast cancer; design, synthesis and molecular docking. RSC Adv. 2024 Jul 12;14(31):22092-22112. doi: 10.1039/d4ra04371e. PMID: 39005243; PMCID: PMC11240139
5. Kumar C P, Banumathi, Satyanarayan ND, et al. A quinoline derivative exerts antineoplastic efficacy against solid tumour by inducing apoptosis and anti-angiogenesis both in vitro and in vivo. Naunyn-schmiedeberg's Archives of Pharmacology. 2025 Jul;398(7):9161-9176. DOI: 10.1007/s00210-025-03830-8. PMID: 39912901
6. Mannino G, Serio G, Asteggiano A, Gatti N, Bertea CM, Medana C, et al. Bioactive Compounds and Antioxidant Properties with Involved Mechanisms of *Eugenia involucrata* DC Fruits. Antioxidants (Basel). 2022 Sep 7;11(9):1769. doi: 10.3390/antiox11091769. PMID: 36139843; PMCID: PMC9495894.
7. Prasad R Sakshith, Satyanarayan Nayak, Shetty Avarse, Basaiah, Thippeswamy. Synthesis, antimicrobial, and antitubercular evaluation of new Schiff bases with in silico ADMET and molecular docking studies. European Journal of Chemistry. 2022;13:109-116. 10.5155/eurjchem.13.1.109-116.2216
8. Meshginfar N, Sadeghi Mahoonak A, Hosseinian F, Ghorbani M, Tsopmo A. Production of antioxidant peptide fractions from a by-product of tomato processing: mass spectrometry identification of peptides and stability to gastrointestinal digestion. *J Food Sci Technol*. 2018;55(9):3498-3507. doi:10.1007/s13197-018-3274-z
9. Megha Gowri Thippeswamy, Rajeshwara Achur, Ravikumar Hemagirigowda, Manjunatha Daddayya, Thoyajakshi Ramasamudhra Siddaraju, Shridhar Mathad, et al. Next generation sequencing identified bio-active peptides: Evaluation of its in vitro, in vivo and in silico anti-inflammatory activities. Results Chem. 2025; 16:102372, ISSN 2211-7156, https://doi.org/10.1016/j.rechem.2025.102372
10. History Article, Ayodele Peter. Bamigbade Adekunle, Bamigbade Ololade, Adeniyi Isaac, Tachin Esther, et al. Illustrated Procedure to Perform Molecular Docking Using PyRx and Biovia Discovery Studio Visualizer: A Case Study of 10kt With Atropine. PDDBS. 2023;6:1-32. 10.36877/pddbs.a0000424
11. Huang J, MacKerell AD Jr. CHARMM36 all-atom additive protein force field: validation based on comparison to NMR data. J Comput Chem. 2013 Sep 30;34(25):2135-45. doi: 10.1002/jcc.23354. Epub 2013 Jul 6. PMID: 23832629; PMCID: PMC3800559.
12. Bauer P, Hess B, Lindahl E. GROMACS 2022.4 Manual. 2022. doi:10.5281/ZENODO.7323409
13. Vanommeslaeghe K, Hatcher E, Acharya C, Kundu S, Zhong S, Shim J, et al. CHARMM general force field: A force field for drug-like molecules compatible with the CHARMM all-atom additive biological force fields. J Comput Chem. 2010

Mar;31(4):671-90. doi: 10.1002/jcc.21367. PMID: 19575467; PMCID: PMC2888302
14. Darden T, York D, Pedersen L. Particle Mesh Ewald: An N ·log(N) Method for Ewald Sums in Large Systems. The Journal of Chemical Physics 1993;98:10089–10092. doi:10.1063/1.464397
15. Harrach MF, Drossel B. Structure and dynamics of TIP3P, TIP4P, and TIP5P water near smooth and atomistic walls of different hydroaffinity. J Chem Phys. 2014 May 7;140(17):174501. doi: 10.1063/1.4872239. PMID: 24811640.
16. Hess Berk, Bekker Henk, Berendsen Herman, Fraaije Johannes. LINCS: A Linear Constraint Solver for molecular simulations. Journal of Computational Chemistry. 1998;18. DOI:10.1002/(SICI)1096-987X(199709)18:123.0.CO;2-H
17. Bussi G, Donadio D, Parrinello M. Canonical sampling through velocity rescaling. J Chem Phys. 2007 Jan 7;126(1):014101. doi: 10.1063/1.2408420. PMID: 17212484
18. Martoňák R, Laio A, Parrinello M. Predicting Crystal Structures: The Parrinello-Rahman Method Revisited. Phys. Rev. Lett. 2003;90:075503. doi:10.1103/PhysRevLett.90.075503
19. Maisuradze GG, Liwo A, Scheraga HA. Relation between Free Energy Landscapes of Proteins and Dynamics. J Chem Theory Comput 2010;6:583–595. doi:10.1021/ct9005745
20. Valdés-Tresanco MS, Valdés-Tresanco ME, Valiente PA, Moreno E. gmx_MMPBSA: A New Tool to Perform End-State Free Energy Calculations with GROMACS. J. Chem. Theory Comput. 2021;17:6281–6291. doi:10.1021/acs.jctc.1c00645
21. Miller BRI, McGee TDJr, Swails JM, Homeyer N, Gohlke H, Roitberg AE. MMPBSA.Py: An Efficient Program for End-State Free Energy Calculations. J. Chem. Theory Comput. 2012;8:3314–3321. doi:10.1021/ct300418h
22. Platzer M, Kiese S, Herfellner T, Schweiggert-Weisz U, Miesbauer O, Eisner P. Common Trends and Differences in Antioxidant Activity Analysis of Phenolic Substances Using Single Electron Transfer Based Assays. Molecules. 2021 Feb 25;26(5):1244. doi: 10.3390/molecules26051244. PMID: 33669139; PMCID: PMC7956415
23. Verbanac D, Malik R, Chand M, Kushwaha K, Vashist M, Matijašić M, et al. Synthesis and evaluation of antibacterial and antioxidant activity of novel 2-phenyl-quinoline analogs derivatized at position 4 with aromatically substituted 4H-1,2,4-triazoles. J Enzyme Inhib Med Chem. 2016;31(sup2):104-110. doi: 10.1080/14756366.2016.1190714. Epub 2016 Jun 19. PMID: 27319400
24. Zhang Y, Fang Y, Liang H, Wang H, Hu K, Liu X, et al. Synthesis and antioxidant activities of 2-oxo-quinoline-3-carbaldehyde Schiff-base derivatives. Bioorg Med Chem Lett. 2013 Jan 1;23(1):107-11. doi: 10.1016/j.bmcl.2012.11.006. Epub 2012 Nov 10. PMID: 23206864
25. Li H, Wang H, Wang J, Lin Y, Ma Y, Bu M. Design, synthesis and biological evaluation of novel 5α, 8α-endoperoxide steroidal derivatives with hybrid side chain as anticancer agents. Steroids. 2020 Jan;153:108471. doi: 10.1016/j.steroids.2019.108471. Epub 2019 Aug 7. PMID: 31400390
26. Petros AM, Olejniczak ET, Fesik SW. Structural biology of the Bcl-2 family of proteins. Biochim Biophys Acta. 2004 Mar 1;1644(2-3):83-94. doi: 10.1016/j.bbamcr.2003.08.012. PMID: 14996493
27. Youle RJ, Strasser A. The BCL-2 protein family: opposing activities that mediate cell death. Nat Rev Mol Cell Biol. 2008 Jan;9(1):47-59. doi: 10.1038/nrm2308. PMID: 18097445
28. Richard DJ, Lena R, Bannister T, Blake N, Pierceall WE, Carlson NE, et al. Hydroxyquinoline-derived compounds and analoguing of selective Mcl-1 inhibitors using a functional biomarker. Bioorg Med Chem. 2013 Nov 1;21(21):6642-9. doi: 10.1016/j.bmc.2013.08.017. Epub 2013 Aug 15. PMID: 23993674; PMCID: PMC3831274
29. McHenry MW, Shi P, Camara CM, Cohen DT, Rettenmaier TJ, Adhikary U, et al. Covalent inhibition of pro-apoptotic BAX. Nat Chem Biol. 2024 Aug;20(8):1022-1032. doi: 10.1038/s41589-023-01537-6. Epub 2024 Jan 17. PMID: 38233584; PMCID: PMC11252247
30. Joerger AC, Fersht AR. The tumor suppressor p53: from structures to drug discovery. Cold Spring Harb Perspect Biol. 2010 Jun;2(6):a000919. doi: 10.1101/cshperspect.a000919. Epub 2010 Feb 10. PMID: 20516128; PMCID: PMC2869527
31. Elkaeed EB, Taghour MS, Mahdy HA, Eldehna WM, El-Deeb NM, Kenawy AM, et al. New quinoline and isatin derivatives as apoptotic VEGFR-2 inhibitors: design, synthesis, anti-proliferative activity, docking, ADMET, toxicity, and MD simulation studies. J Enzyme Inhib Med Chem. 2022 Dec;37(1):2191-2205. doi: 10.1080/14756366.2022.2110869. PMID: 35975321; PMCID: PMC9387325.
32. Mishra S, Sachdeva M, Nimesh H. Network Pharmacology and Molecular Docking to Identify the Molecular Targets of Novel Indole-Quinoline Derivative in Cancer. Orient J Chem 2025;41(1). doi.org/10.13005/ojc/410105
33. Ahmad A, Sayed A, Ginnebaugh KR, Sharma V, Suri A, Saraph A, et al. Molecular docking and inhibition of matrix metalloproteinase-2 by novel difluorinatedbenzylidene curcumin analog. *Am J Transl Res*. 2015;7(2):298-308. Published 2015 Feb 15.
34. Trachootham D, Alexandre J, Huang P. Targeting cancer cells by ROS-mediated mechanisms: a radical therapeutic approach? Nat Rev Drug Discov. 2009 Jul;8(7):579-91. doi: 10.1038/nrd2803. Epub 2009 May 29. PMID: 19478820
35. Fulda S, Debatin KM. Modulation of apoptosis signaling for cancer therapy. Arch Immunol Ther Exp (Warsz). 2006 May-Jun;54(3):173-5. doi: 10.1007/s00005-006-0019-x. Epub 2006 May 2. PMID: 16652217
36. Gorrini C, Harris IS, Mak TW. Modulation of oxidative stress as an anticancer strategy. Nat Rev Drug Discov. 2013 Dec;12(12):931-47. doi: 10.1038/nrd4002. PMID: 24287781